

# Observations of the Naked-Eye GRB 080319B: Implications of Nature's Brightest Explosion

J. S. Bloom<sup>1,2</sup>, D. A. Perley<sup>1</sup>, W. Li<sup>1</sup>,  
 N. R. Butler<sup>1</sup>, A. A. Miller<sup>1</sup>, D. Kocevski<sup>1</sup>, D. A. Kann<sup>5</sup>,  
 R. J. Foley<sup>1</sup>, H.-W. Chen<sup>3</sup>, A. V. Filippenko<sup>1</sup>, D. L. Starr<sup>1,4</sup>,  
 B. Macomber<sup>1</sup>, J. X. Prochaska<sup>6</sup>, R. Chornock<sup>1</sup>,  
 D. Poznanski<sup>1</sup>, S. Klose<sup>5</sup>, M. F. Skrutskie<sup>7</sup>,  
 S. Lopez<sup>8</sup>, P. Hall<sup>9</sup>, K. Glazebrook<sup>10</sup>, and C. H. Blake<sup>11</sup>

<sup>1</sup> *Department of Astronomy, University of California, Berkeley, CA 94720-3411.*

<sup>2</sup> *Sloan Research Fellow.*

<sup>3</sup> *Department of Astronomy & Astrophysics, University of Chicago, Chicago, IL 60637.*

<sup>4</sup> *Las Cumbres Global Telescope Network, 6740 Cortona Dr. Santa Barbara, CA 93117.*

<sup>5</sup> *Thüringer Landessternwarte Tautenburg, Sternwarte 5, D-07778 Tautenburg, Germany.*

<sup>6</sup> *University of California Observatories/Lick Observatory, University of California, Santa Cruz, CA 95064.*

<sup>7</sup> *Department of Astronomy, P.O. Box 3818, University of Virginia, Charlottesville, VA 22903-0818.*

<sup>8</sup> *Departamento de Astronomia, Universidad de Chile, Casilla 36-D, Santiago, Chile.*

<sup>9</sup> *Physics and Astronomy, Toronto, Ontario, M3J 1P3, Canada.*

<sup>10</sup> *Centre for Astrophysics and Supercomputing, Swinburne University of Technology, Hawthorn, VIC 3122, Australia*

<sup>11</sup> *Harvard-Smithsonian Center for Astrophysics, 60 Garden Street, Cambridge, MA 02138.*

## ABSTRACT

The first gamma-ray burst (GRB) confirmed to be bright enough to be seen with the naked eye, GRB 080319B at redshift  $z = 0.937$ , allowed for exquisite follow-up observations across the electromagnetic spectrum. We present our detailed optical and infrared observations of the afterglow, consisting of over 5000 images starting 51 s after the GRB trigger, in concert with our own analysis of

the *Swift* UVOT, BAT, and XRT data. The event is extreme not only in observed properties but intrinsically: it was the most luminous event ever recorded at optical and infrared wavelengths and had an exceedingly high isotropic-equivalent energy release in  $\gamma$ -rays. At early times, the afterglow evolution is broadly consistent with being reverse-shock dominated, but then is subsumed by a forward shock at around 1000 s. The overall spectral energy distribution, spanning from ultraviolet through near-infrared wavelengths, shows no evidence for a significant amount of dust extinction in the host frame. The afterglow evolution, however, is highly chromatic: starting at about 1000 s the index shifts blueward before shifting back to the red at late times. In our deepest late-time observations, we find tentative evidence for an optical jet break and a luminous supernova. Finally, we examine the detectability of such events with current and future facilities and find that such an event could be detected in gamma-rays by BAT out to  $z = 10.7$  ( $8\sigma$ ), while the nominal EXIST sensitivity would allow detection to  $z \approx 32$ . At  $K$  band, this source would have been easily detected with meter-class telescopes to  $z \approx 17$ .

*Subject headings:* gamma rays: bursts, gamma-ray bursts: individual: 080319B

## 1. Introduction

The longevity and burst-discovery prowess of the *Swift* mission (Gehrels et al. 2004) has led to a boom in correlative studies of the properties of a large sample of gamma-ray bursts (GRBs) observed systematically and uniformly. At the same time, the sheer number of bursts encompasses an ever-expanding volume of interesting parameter space, often revealing rarities that help to redefine and shape the totality of our understanding of the phenomenon. It is in the backdrop of the latter that GRB 080319B superlatively reigns.

At 06:12:49 (UTC is used throughout this paper), GRB 080319B triggered (Racusin et al. 2008a) the *Swift* Burst Alert Telescope (BAT), the second GRB trigger that day in what would be 5 GRB triggers in a 24 hr period. The extreme brightness of the burst at high energies, in the X-ray afterglow, and in the ultraviolet/optical/infrared (UV/O/IR) afterglow led to a flurry of follow-up observations, many automatically triggered on robotic facilities. Contemporaneous imaging, both all-sky and directed, uncovered a fast-rising optical afterglow which peaked a time from trigger of  $t \approx 18.3$  s at  $V \approx 5.3$  mag (Cwiok et al. 2008a; Covino et al. 2008; Swan et al. 2008; Karpov et al. 2008a; Schubel et al. 2008; Wozniak et al. 2008); this makes the afterglow of GRB 080319B the first confirmed counterpart that could have been seen with the unaided eye in dark skies.

At a redshift of  $z = 0.937$  (Vreeswijk et al. 2008), the event was relatively nearby compared to the *Swift* distribution of long-duration events (e.g., Jakobsson et al. 2006; Daigne et al. 2006; Le & Dermer 2007), yet near the median for redshifts of pre-*Swift* events. One aim of this article is to place the observed properties (particularly energetics) in the context of both distributions; we show in §3 that GRB 080319B was not only potentially the highest-fluence event ever observed, it also had an isotropic-equivalent energy release comparable to the highest known values yet recorded. The other significant aim is to analyze in detail our long-wavelength observations, in both the optical and IR, with high time cadence on moderate-sized robotic telescopes. The quality of the data, coupled with those available in the literature and from public archives, reveals a complex evolution of the afterglow that we attempt to reconcile with canonical afterglow theory. Unless noted, we assume a concordance cosmology with  $H_0 = 71 \text{ km s}^{-1} \text{ Mpc}^{-1}$ ,  $\Omega_\Lambda = 0.70$ , and  $\Omega_m = 0.3$ . A redshift of  $z = 0.937$  corresponds to a luminosity distance of 6011.3 Mpc (distance modulus 43.89 mag). All of the results presented herein, though generally consistent with our previous results in GCN Circulars<sup>1</sup>, supersede them.

## 2. Optical/IR Observations and Reductions

### 2.1. PAIRITEL

The Peters Automated Infrared Imaging Telescope (PAIRITEL; Bloom et al. 2006), responding automatically to the *Swift* trigger via an open-source package<sup>2</sup> connected to the GCN, began taking data on the field at 06:13:39.7 ( $t = 51 \text{ s}$  after the *Swift* trigger). The 1.3 m telescope is equipped with NICMOS3 arrays to simultaneously observe in bands  $J$ ,  $H$ , and  $K_s$  (1.2, 1.6, and 2.2  $\mu\text{m}$ , respectively). Each image consists of a  $256 \times 256$  pixel array with a scale of  $2'' \text{ pixel}^{-1}$ . Data are obtained as a double-correlated read, with a 51 ms accumulation since reset on the first (“short”) read and 7.851 s on the second (“long”) read. Both the long and the short read exposures are saved to disk. The telescope is dithered by  $\sim 1'$  after every third exposure. With no shutter, the standard reductions necessarily incorporate per-pixel models of the combined detector dark current and sky flux fitted over time (Wood-Vasey et al. 2007). In a modified version of our automated pipeline, once these time-specific frames (“sky+dark”) are subtracted from the object frames, they are combined into 3–12 file intermediate mosaics with effective integration times of 24–96 s per image, which in turn are stacked to form the final mosaics.

---

<sup>1</sup><http://gcn.gsfc.nasa.gov/>.

<sup>2</sup><http://sourceforge.net/projects/pygcnssock>.

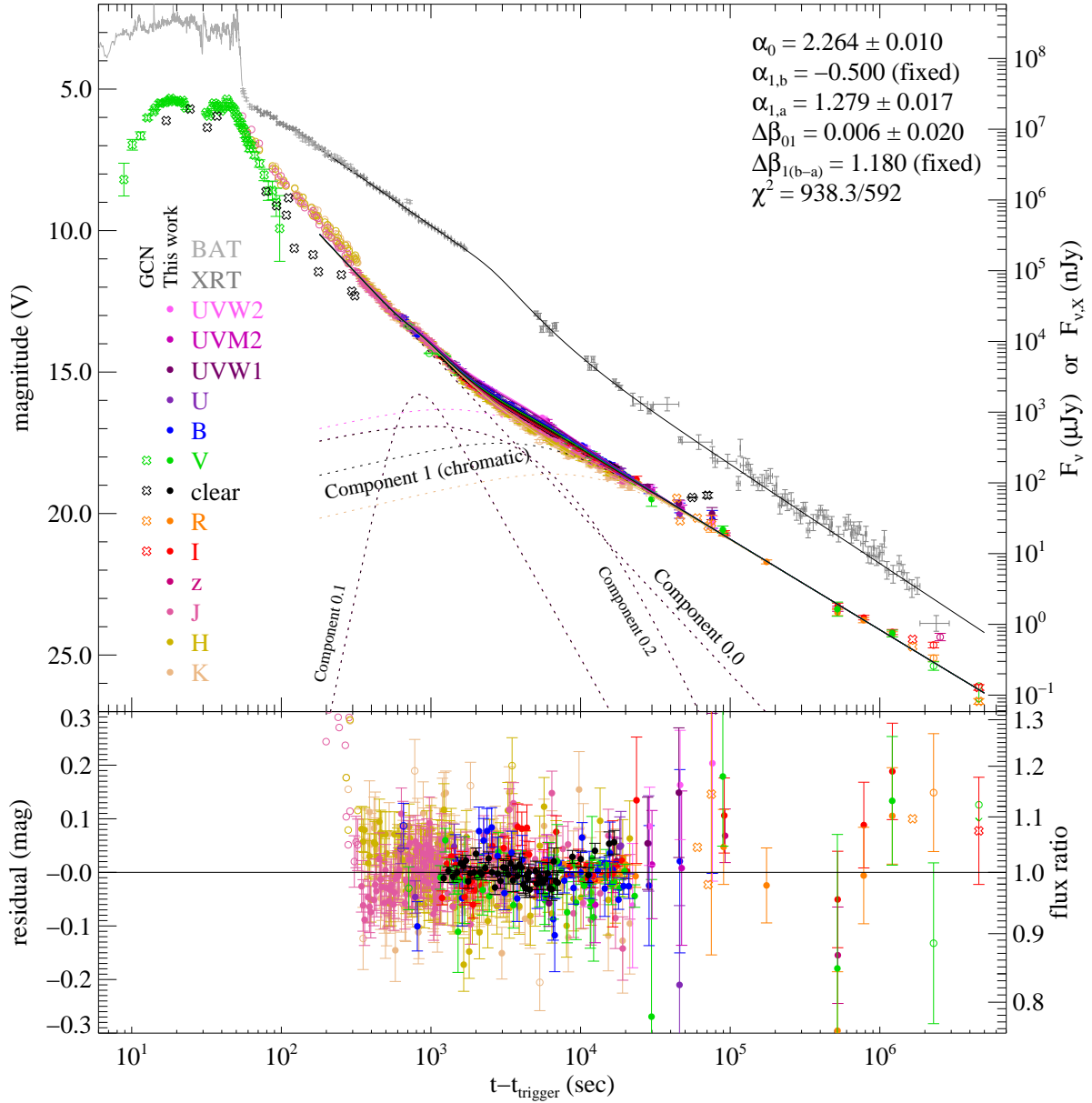


Fig. 1.— Light curves of the GRB 080319B long-wavelength afterglow, fit by our empirical model, which allows (and in this case prefers) color change. This is a combination of data from the GCN Circulares ( $\times$  symbols, including the prompt light curve as plotted by Karpov et al. 2008b, in green), our observations from various ground-based instruments (KAIT, the Lick Nickel 1m, and PAIRITEL) and our re-reductions of the *Swift* UVOT, XRT, and BAT data. The afterglow decays extremely rapidly, dropping from mag 5 to 21 in less than one day. For clarity, UV/O/IR data are corrected to  $V$  [Vega] mag using the model. Individual broken power-law components are shown as dotted lines; these are summed together to generate the fitted model (solid line). Different colors indicate different filters. Empty points were not used in the fitting in §3.4.

During the first few minutes on target (253 s in  $J$ , 289 s in  $H$ , and 289 s in  $K_s$ ), the afterglow was saturated in the exposures, where we have adopted the saturation/non-linearity threshold determined from data for the 2MASS South camera<sup>3</sup>: 37000 counts in a single pixel in the  $J$  and  $H$  bands, and 33000 counts in a single pixel in the  $K_s$  band. In addition, a number of the final science frames suffered from poor sky+dark-frame subtraction and could not be photometered or included in the final mosaics. These frames were removed following an inspection by eye prior to the construction of the final mosaics. Less than 4% of the 7.8 s exposures were removed following this procedure.

Our initial IR photometry report (Bloom et al. 2008) noted that the afterglow had been strongly detected simultaneously in all three filters during the first few minutes of observations. Indeed, the ability to detect the transient in single 7.8 s exposures lasted for a few hours. In total, we obtained 1822 simultaneous  $J$ ,  $H$ , and  $K_s$  observations of the GRB (5466 total frames) over the course of 6 hr, though as the afterglow begins to fade we bin together individual frames to increase the signal-to-noise ratio and improve readability of the light curve.

### 2.1.1. *Photometry on Unsaturated Frames*

A custom pipeline was used to perform photometry on the 7.8 s exposures constructed from the difference of the two readouts which occurred 7.851 and 0.051 s following array reset. This pipeline was also used on the intermediate mosaics constructed from the 7.8s frames. Zeropoint determinations were made in comparison to the 2MASS catalog. The statistical uncertainties are small, while the total uncertainty on any individual image is dominated by systematics, especially at early times, associated with our ability to accurately zeropoint relative to 2MASS. We quantify this systematic uncertainty empirically by measuring the photometric scatter in a mag 10 star (hereafter “S1”), located at  $\alpha = 14^{\text{h}}32^{\text{m}}03^{\text{s}}.55$ ,  $\delta = +36^{\circ}18'29''.6$  (J2000), a few arcmin from the position of the GRB optical afterglow (OA). In all three bands the systematic contribution is  $\sim 4\%$ . The resulting light curves are presented in Figs. 1–2 and listed in Table 1.

---

<sup>3</sup>[http://www.ipac.caltech.edu/2mass/releases/allsky/doc/sec4\\_2.html](http://www.ipac.caltech.edu/2mass/releases/allsky/doc/sec4_2.html) .

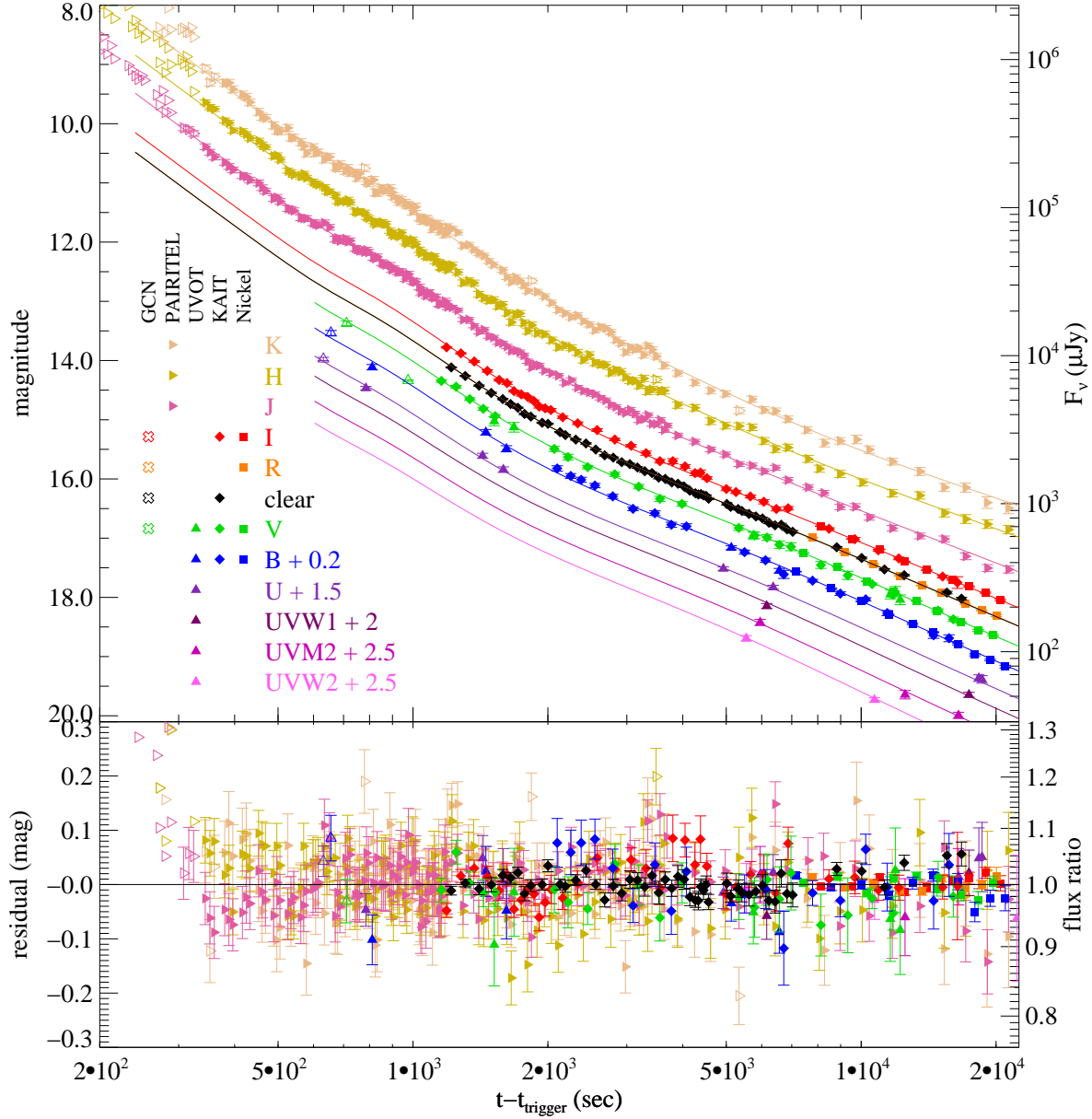


Fig. 2.— Detailed optical-IR light curve covering much of the first night after the afterglow, demonstrating the exquisite time sampling and overall goodness-of-fit of the model. The earliest-time PAIRITEL observations are saturated/non-linear and uncertain (see §2.1.1); these are not included in fitting or modeling.

### 2.1.2. Photometry on Early-Time Imaging

Due to the extreme brightness of the early afterglow, a large number of early PAIRITEL frames are highly saturated or otherwise nonlinear (when the magnitude is  $\lesssim 9$ ). We employed two methods to recover the photometry in these early epochs (see Tables 2–3). First, since there is sufficient signal in the 51 ms short reads to detect the GRB well above the noise when  $JHK_s \gtrsim 7$ , we use the procedure described in Eisner et al. (2007) to extract the flux from the GRB in the short reads and calibrate this to the 2MASS system using stars in the corresponding long reads. The uncertainty of these measurements is primarily dominated by the determination of the zeropoint. Second, we developed a simple method to extract photometry from saturated “long minus short” frames, using an annulus centered on the GRB position. We use S1 to determine the zeropoint for each of the individual saturated long minus short (7.8 s) frames. The inner annulus radius was chosen to exclude any saturated pixels in any frame, while the outer annulus radius was selected to provide sufficient signal without including too much noise as the wings of the point-spread function (PSF) become dominated by noise from the background. The accuracy of these early measurements of the GRB afterglow is strongly limited by the determination of the zeropoint: high near-IR backgrounds and the annulus aperture lead to a large scatter in the determined zeropoints for each frame. Thus, the uncertainty for these early measurements is dominated by a large systematic term, defined as the scatter of the individual zeropoints. We include these points in early-time light-curve plots and in our data table to show the general early behavior of the IR afterglow, but do not include them in any fitting or model analysis. We emphasize that photometry of these saturated frames is subject to unaccounted-for systematic uncertainties, but note qualitative agreement with other submitted early IR imaging (Racusin et al. 2008b).

## 2.2. KAIT and Nickel

At Lick Observatory, the Katzman Automatic Imaging Telescope (KAIT; Filippenko et al. 2001) GRB alert system (Li et al. 2003) responded to GRB 080319B automatically. While ordinarily the time to slew is  $< 1$  min, since KAIT was following GRB 080319A (which triggered *Swift* 30 min earlier) our first observations of GRB 080319B did not start until 19 min after the BAT trigger. We followed the GRB OA with a combination of filters (*BVI* and unfiltered) and with varying exposure times (20 s initially, then 40 s, then 300 s guided exposures), and continued until 280 min after the BAT trigger. We also observed GRB 080319B with the Lick 1-m Nickel telescope remotely from the University of California, Berkeley, between 116 and 392 min after the BAT trigger, using *BVRI* filters and exposure times of

300 s and 360 s.

To reduce the KAIT and Nickel data, we used the PSF-fitting technique in IRAF/DAOPHOT. Instrumental magnitudes were measured for the GRB OA and several local standard stars, and conversion to the standard  $BVRI$  system was accomplished using the SDSS calibration (Cool et al. 2008; Adelman-McCarthy et al. 2008) of the field (the magnitudes in the SDSS magnitude system were converted to  $BVRI$  following the recipe of Lupton 2005<sup>4</sup>). Two of the SDSS standards in our field are shared with the standard star calibration of Henden (2008); because the posted magnitudes for both stars are consistent within the uncertainties, we adopted the SDSS system due to the much larger number of stars and the ability to extend to deep late-time observations. The final KAIT and Nickel photometry is listed in Tables 4 and 5. A list of the converted  $BVRI$  magnitudes of the bright standards used in this calibration is given in Table 9.

### 2.3. UVOT

To extend the wavelength coverage, we downloaded the *Swift* UVOT data from the quicklook data archive. The Level 2 sky image data in  $U$ ,  $B$ , and  $V$  were analyzed according to the photometry calibration and recipe by Li et al. (2006). We also followed the procedure reported in Poole et al. (2008), and found that when the GRB was bright, the two procedures yield similar results. When the GRB became faint, the Li et al. (2006) procedure yields measurements with smaller uncertainties and better overall agreement with the KAIT and Nickel data in the  $B$  and  $V$  passbands, likely due to the smaller adopted photometry aperture. The *Swift* UV filters ( $UVW1$ ,  $UVM1$ , and  $UVW2$ ) were reduced following Poole et al. (2008). The final UVOT photometry is reported in Table 6.

### 2.4. Gemini Spectroscopy

An optical spectrum of GRB080319B was obtained under program GS-2008A-Q-20 beginning at 08:23 on 19 Mar. 2008 (Cwiok et al. 2008b) using the Gemini South 8-m telescope with GMOS (Hook et al. 2004). We used a slit of width  $0.75''$ , the R831 grating, and a OG515 filter. Two 1800 s exposures were obtained with slightly different central wavelengths of 7000 and 7100 Å and read out in  $2 \times 2$  binning. Standard CCD processing and

---

<sup>4</sup><http://www.sdss.org/dr6/algorithms/sdssUBVRITransform.html#Lupton2005>.



spectrum extraction were accomplished with IRAF (for more details, see Foley et al. 2006). The data were extracted using the optimal algorithm of Horne (1986). The spectrum shows a featureless continuum with no strong absorption systems, emission features, or spectral breaks. Unfortunately, our wavelength range does not cover the spectral range of the VLT spectrum where strong absorption features were seen (Vreeswijk et al. 2008). With our spectral coverage, and given the proposed redshift of GRB 080319B (Vreeswijk et al. 2008), the strongest ISM absorption lines for a galaxy at  $z = 0.937$  are expected to be Ti II 3384 and the Ca II doublet at  $\lambda \approx 3950\text{\AA}$ . We do not detect Ti II  $\lambda 3384$  to a  $3\sigma$  rest-frame absorption equivalent width limit of  $W = 0.05\text{\AA}$  over a spectral resolution element, while the Ca II H & K absorption doublet is blended with the atmospheric A-band absorption. No additional features were found in our observed wavelength range of 5950–8150  $\text{\AA}$ .

## 2.5. Gemini Imaging

In the nights following the burst, we began a program of additional imaging using Gemini South and Gemini North. On the first night following the event, we acquired  $4 \times 180$  s of GMOS imaging in each of the  $g$ ,  $r$ ,  $i$ , and  $z$  filters under excellent seeing conditions ( $0.85''$ ) despite the low elevation of the target (airmass of 2.5). A second epoch was acquired the following night in  $r$  only, and additional multicolor epochs were taken later on March 25 and 28, and April 2. Imaging was taken at Gemini North on April 14 ( $g$ ,  $r$ ,  $i$ ) and 17 ( $z$ ). Data were reduced using the standard Gemini IRAF package and photometered using SExtractor (Bertin & Arnouts 1996) aperture magnitudes. The field was calibrated relative to select stars from SDSS DR6 (Adelman-McCarthy et al. 2008, Table 10). The Gemini filters appear to be somewhat nonstandard compared to the SDSS survey filters, so significant color-term corrections were necessary. As the number of comparison stars used was large we were able to calculate these individually for each observation. The color dependence is about 20% in  $g$  on Gemini North and 30% on Gemini South. In  $r$ ,  $i$ , and  $z$  it is about 10%, 15%, and 5% (respectively) on both telescopes. The final photometry is given in Table 7. For use in the light-curve fitting (for which a comparison to the early-time  $BVRI$  observations is necessary), the  $gri$  magnitudes for the afterglow were then converted back to  $VRI$  using the equations of Lupton (2005).

## 2.6. GCN Circulars

Finally, to supplement our data at very early times and late times, we downloaded additional photometry from the GCN Circulars. Of particular note, we downloaded the

corrected TORTORA light curve (Karpov et al. 2008b) containing high-quality optical photometry throughout the prompt phase, and *Hubble Space Telescope (HST)* data points at late times (Tanvir et al. 2008; Levan et al. 2008), which allow us to complete the entire light curve of this event. Due to the fact that GCN observations are preliminary and may have large calibration offsets, we do not use any of the GCN points in any of our fits or models, though we do show them in light-curve plots. Instead, we focus our analysis on the intermediate phase of the burst, from 300 s to  $10^6$  s, during which we have good time sampling. The GCN data shown in our plots are listed in Table 8.

## 2.7. Swift BAT and XRT

Our high-energy reduction pipeline is described in detail by Butler et al. (2007) for the *Swift* BAT and by Butler & Kocevski (2007a) for the *Swift* XRT. GRB 080319B exhibits one dominant emission episode of duration  $\Delta t \approx 60$  s, composed of multiple unresolved spikes. The BAT spectrum in the time interval  $-1.1$  s to 57.4 s is acceptably fit ( $\chi^2/\nu = 13.55/55$ ) by a simple power law with photon index  $\alpha = -1.01 \pm 0.02$  and energy fluence  $(1.96 \pm 0.03) \times 10^{-4}$  erg cm $^{-2}$  (15–350 keV). The BAT catches only the low-energy portion of a spectrum extending beyond  $E_{\text{peak,obs}} = 651_{-14}^{+13}$  keV (Golenetskii et al. 2008), with an isotropic-equivalent energy release in  $\gamma$ -rays of  $\sim 10^{54}$  erg. There is evidence for a gamma-ray tail detected up to  $\sim 1000$  s as seen in Fig. 1. This extended emission at late times is similar to that observed in the extremely bright BATSE GRB 980923 (Giblin et al. 1999) and *Swift* GRB 061007 (Mundell et al. 2007; Schady et al. 2007a).

The *Swift* XRT began observing during the tail of the prompt emission phase at  $t = 66$  s. We find (see, also, Butler 2008) that the X-ray spectrum is unchanging until quite late times ( $t = 2.91$  Ms) despite a break in the X-ray light curve at  $t \approx 1$  ks (Fig. 1). The combined XRT/BAT data are well fit by an absorbed power law with  $\Gamma = 1.814 \pm 0.011$  and an excess column density over Galactic of  $N_{\text{H}} = (1.87 \pm 0.13) \times 10^{21}$  cm $^{-2}$  at  $z = 0.937$ . The early-time windowed timing (WT) mode ( $66 \text{ s} < t < 4.95 \text{ ks}$ ) X-ray photon index  $\Gamma_1 = 1.814 \pm 0.013$  is closely consistent with the late-time photon-counting (PC) mode ( $4.95 \text{ ks} < t < 2.91 \text{ Ms}$ ) X-ray photon index  $\Gamma_2 = 1.80 \pm 0.04$ , assuming a constant  $N_{\text{H}}$ . From negligible  $\lesssim 1\%$  variations in the X-ray hardness ratio (see, e.g., Butler & Kocevski 2007b), the magnitude of any secular trends in  $\Gamma_1$  or  $\Gamma_2$  must be at the few-percent level or less, and there is no evidence for variation in  $N_{\text{H}}$ .

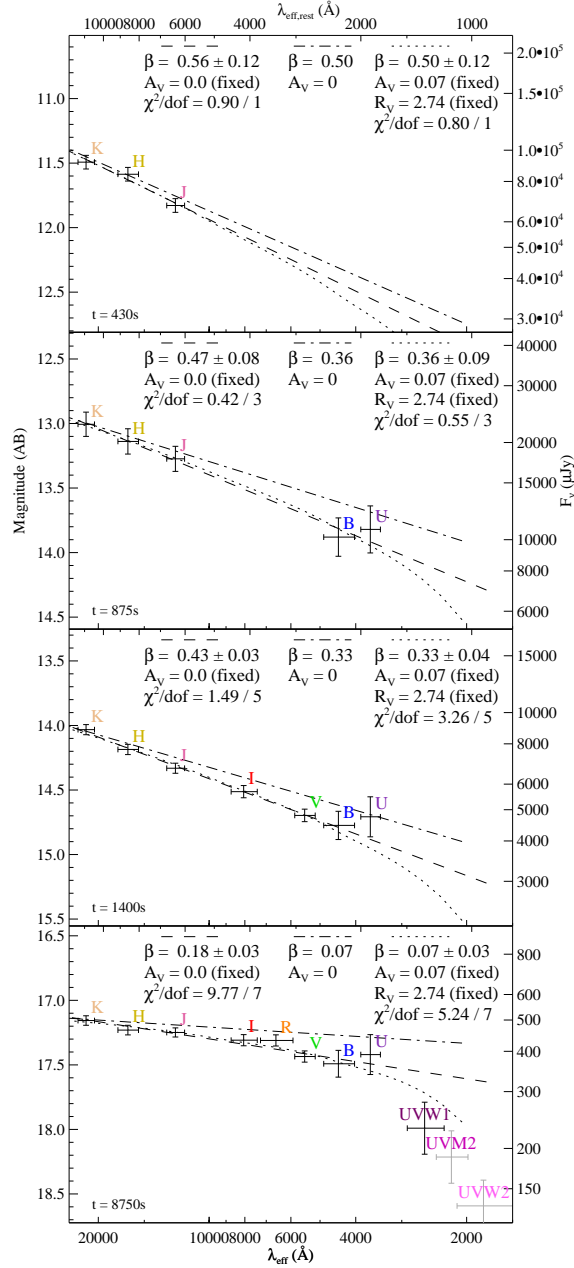


Fig. 3.— Photometric spectral energy distributions (SEDs) generated over specific time ranges during the first night after the burst from combined PAIRITEL, KAIT, Nickel, and UVOT measurements. All plots have the same horizontal and vertical scale, differing only in the vertical offset. The assumed host-galaxy extinction is based on a fit using a combined SED from all epochs (a fit assuming no host extinction is also shown for comparison). A clear red-to-blue transition is evident during this time. The three lines show the various fits to the data with the relevant parameters noted. “Fixed” indicates that that parameter is held constant in the fit.

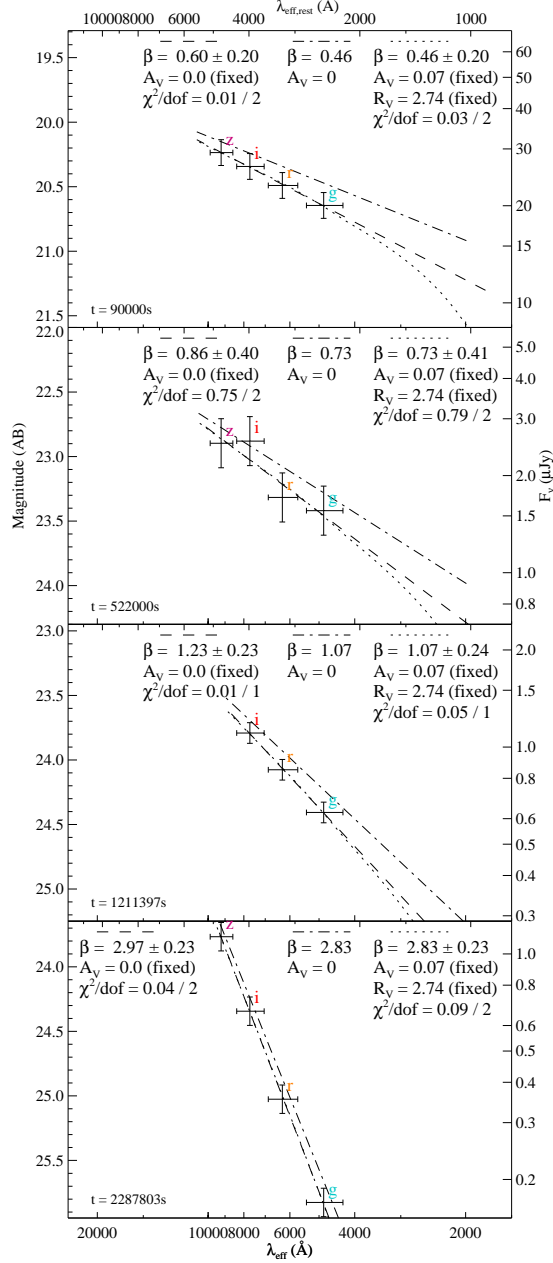


Fig. 4.— Photometric SEDs generated on subsequent nights from multicolor Gemini South and Gemini North observations. The scale and assumed host extinction are the same as in Figure 3. The color is consistent with constant evolution early, but shifts dramatically redward at very late times, likely due to the appearance of a very luminous supernova.

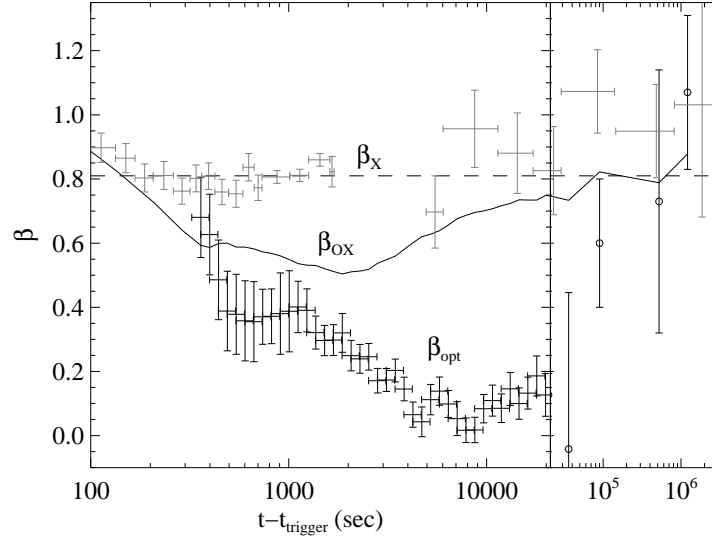


Fig. 5.— Evolution of the afterglow spectral index  $\beta$  with time. The optical spectral index  $\beta_{\text{opt}}$  is measured from a fit to the UV-optical-IR data from each of 40 different overlapping bins ranging from 360 s to 22000 s, plus one additional series of UVOT exposures and the first three multicolor Gemini epochs. The X-ray spectral index is also plotted (gray points), with the dashed line showing the best-fit value assuming no spectral evolution (which the data are consistent with). The optical-to-X-ray spectral index  $\beta_{\text{OX}}$  is defined as the index between the X-ray (normalized at 1 keV) and the  $V$ -band optical flux. At early times the optical spectral index evolves from red to blue to red again. The X-ray, optical, and optical-to-X-ray spectral indices are all consistent at late times, which may suggest that both optical and X-ray bands are in the same synchrotron regime.

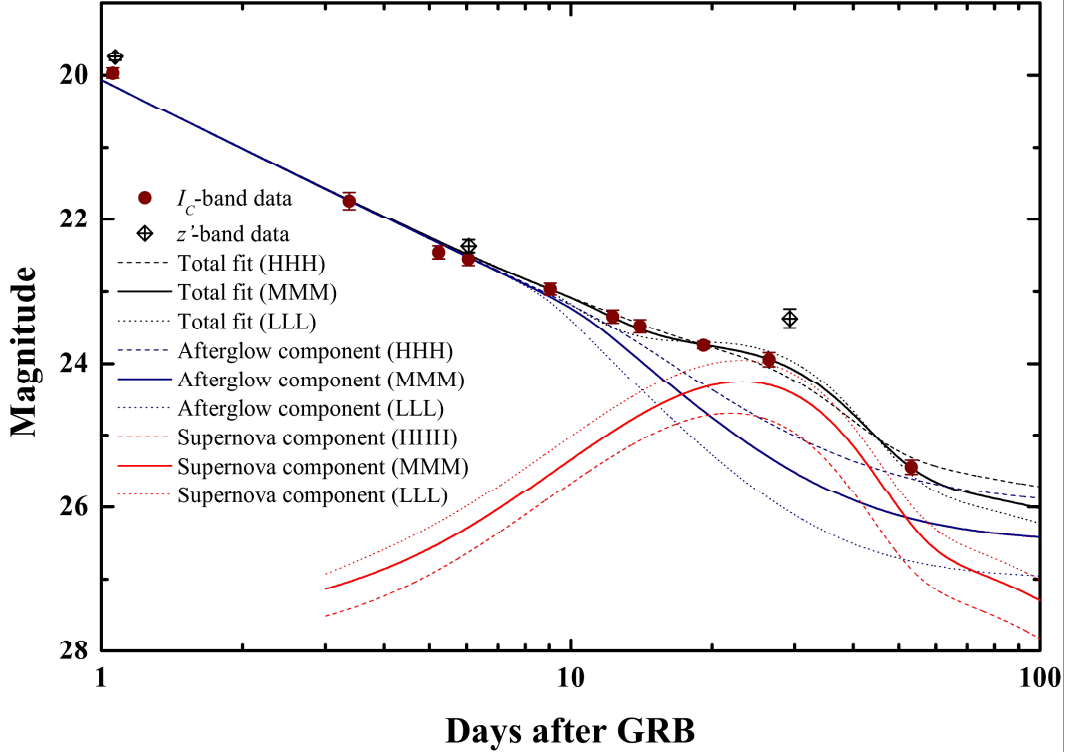


Fig. 6.— Fits to the late-time  $I_C$ -band data with a combination of an afterglow component described with a broken power-law, a constant host galaxy component and a supernova component. We assume that the late afterglow, in terms of break-time ( $11.5 \pm 3$  day) and post-break decay slope ( $2.45 \pm 0.35$ ), follows the values derived from the X-ray afterglow (the pre-break decay slope is left free to vary, but is strongly constrained by earlier data which is not plotted). The black lines represent the sum of all components, directly fit to the data. The blue lines give the afterglow plus host galaxy component, whereas the red lines show the supernova contribution. Unbroken lines denote the use of the central values (M for Mid) derived from the X-ray fit and a host galaxy magnitude of  $I_C = 26.5$ . Dotted lines denote the extreme (L)ow case of the (within  $1\sigma$  errors of the X-ray fit) earliest break and steepest post-break decay slope, as well as the faintest host galaxy (where we choose conservative errors of 0.5 magnitudes). In this case, at late times, the supernova dominates the afterglow. The dashed lines denote the opposite case (H for High), a late break and shallow post-break decay as well as a bright host galaxy, which results in the smallest supernova contribution, comparable to the afterglow at peak. Even so, we find this “faint” supernova component to be 50% more luminous than SN 1998bw at peak. We also plot the three  $z'$  observations. The two first points show no color evolution, whereas the last point is significantly brighter than the extrapolated  $I_C$  light curve and gives further evidence of the strong reddening due to the rising supernova component.

### 3. Analysis

#### 3.1. Optical Light Curve

We fit the optical data in all filters simultaneously by fitting a series of summed Beuermann et al. (1999) functions, a generalization of the procedure described by Perley et al. (2008). Several iterations of different models with varying assumptions and complexity were fitted, with our final preferred model motivated by a combination of assumptions of underlying physical behavior (as will be described shortly) and the necessity to fit the data with a reasonable  $\chi^2$  and without large trends in the residuals. This model contains two elements: a monochromatic, rapidly falling component which dominates at early times ( $\lesssim 10^4$  s), plus a chromatically evolving second component which peaks at about  $10^3 - 10^4$  s (depending on the filter). The first component is actually a sum of three Beuermann functions (this was necessary to fit several low-level modulation “wiggles” in the data); the second component is a single Beuermann function, but the peak time is allowed to be a function of the filter central wavelength to allow the break (peak) to be chromatic. (Modulations are seen at late times as well, but we do not have the temporal coverage to accurately attempt to characterize them.) We exclude points after  $2 \times 10^6$  s, which appear to be contaminated by additional light (possibly due to a supernova; see §3.7) in most filters. We use only our own calibrated data; observations reported in the GCN Circulars are excluded from the fits. Very early points from UVOT and PAIRITEL that were heavily affected by pileup, saturation, or nonlinearity effects were excluded, and a small number of other conspicuous outliers at late times were manually flagged during the fitting process.

Our model is found to match the data very well, with no obvious residual trends, with the exception of a possible chromatic divergence of the very early-time IR measurements from the initial power law. The final value for  $\chi^2 = 938$  (over 592 degrees of freedom) is reasonable, if not strictly statistically acceptable, although this is not necessarily a surprise given the large number of different instruments and very complicated behavior of the afterglow. A modest underestimate of the systematic errors could account for  $\chi^2/\text{dof} > 1$ . All optical photometry from our measurements and the GCN Circulars is presented in Figure 1. Here we adopt the convention for the spectral index ( $\beta$ ) and the temporal index ( $\alpha$ ) such that  $f_\nu \propto \nu^{-\beta} t^{-\alpha}$ . A subset of these observations showing our measurements in more detail is shown in Figure 2.

The early afterglow decay is extremely rapid:  $\alpha \approx 2.24$ . At about 500 s the light curve flattens slightly, and then levels out much more significantly around 1500 s, as noted by Li et al. (2008). Our rapid temporal sampling ends at 20,000 s due to bright morning twilight, but we began Gemini observations the following night, and from then until about

$10^6$  s the optical afterglow decays approximately as a simple power law, although some limited achromatic variations both above and below the fit may suggest small modulations.

Our fitting procedure is capable of assigning different colors to different components and modeling chromatic breaks, so there is no need to assume achromatic evolution. Indeed, attempts at monochromatic fits invariably produced very poor  $\chi^2$  values and obvious residual trends, and color evolution is clear in the time-dependent SED (§3.2). Our final preferred model is able to fit all the chromatic evolution using the chromatic break of the late-time component, which transitions from blue (while rising) to red (while fading). This behavior is strongly reminiscent of the predicted evolution of a forward shock at peak, so we fix the rising power-law index  $\alpha_{1,b}$  and the overall color change over the break  $\Delta\beta_{1,b-a}$  to the values predicted by this model. (They are nearly unconstrained by the fits otherwise.) This late-time component is allowed to have a different post-break color from the early-time component, but the fits suggest they have similar values, with the overall beginning-to-end change in spectral index of  $\Delta\beta = 0.006 \pm 0.020$ , despite a notable color change in the intermediate region.

### 3.2. SED and Extinction Constraints

Due to the excellent coverage of the photometry across the UV/O/IR spectrum, we can strongly constrain the host-galaxy extinction. Our chromatic model can generate SEDs at any point in the evolution of the light curve using all available filters, shielding us from the possibility that the intrinsic (pre-extinction) SED may not be a simple power law during the periods when most of the observations were actually taken (though only to the extent to which our model accurately describes the light curve). We can therefore use all available filters to fit a single extinction law to the full data in spite of the observed chromatic behavior. After correcting for the small Galactic extinction along this sightline of  $E(B-V) = 0.01$  mag (Schlegel et al. 1998) and excluding the Swift UVM2 and UVW2 filters (which are likely to be significantly affected by Lyman- $\alpha$  and Lyman-break absorption, respectively), we measure  $A_{V,\text{host}} = 0.07 \pm 0.06$  mag for a fit to the Small Magellanic Cloud (SMC) extinction law. Milky Way Galaxy and Large Magellanic Cloud (LMC) laws were also tried, but generally had higher values of  $\chi^2$  — to be sure, the small amount of extinction makes the exact choice of extinction law unimportant. Due to the possibility of hydrogen absorption and the generally uncertain nature of extinction laws in the far UV, the UVW2 and UVM2 filters were excluded from these fits. Compared to the X-ray host-galaxy hydrogen column of  $N_{\text{H}} = (1.87 \pm 0.13) \times 10^{21} \text{ cm}^{-2}$ , this suggests a dust-to-gas (actually dust-to-free-metals) ratio of about ten times the Galactic value, which is typical for previous GRB sightlines



(e.g., Schady et al. 2007b). The small amount of extinction inferred is also typical (e.g., Kann et al. 2006).

We can also generate purely observational time-dependent SEDs. The photometric observations taken the night of the burst were divided into 40 overlapping regions, and a simple power law was fit to the magnitudes in each region in order to produce contemporaneous observed fluxes in each available filter at each region. Galactic extinction, as well as the small amount of host extinction correction found above, are removed, and each SED is then fit to a power law to estimate the overall UV/O/IR spectral index  $\beta$  as a function of time. Some representative epochs are shown in Figure 3. These are supplemented by SEDs generated directly from the late-time Gemini observations (with a small correction owing to the fact that different filters were not observed exactly contemporaneously), shown in Figure 4. Finally, we can combine all available data to plot the spectral index  $\beta$  as a function of time, as shown in Figure 5. The chromatic behavior of this afterglow is immediately evident.

### 3.3. X-ray Fits

We employ a similar fitting procedure to the X-ray light curve as in the optical and distinguish two distinct components: a smooth early decay of  $\alpha = 1.48$  breaks at 2500 s to a short lived and poorly constrained (due to lack of observations during this period) fast decay of  $\alpha \approx 2.8$ , and then declines as  $\alpha = 1.40$  for the remainder of its evolution (possibly except for the last observation in which the afterglow is detected, which appears to be significantly below this curve). This differs from the optical value by  $\Delta\alpha = 0.17$ . Toward the very end of the XRT observations, the flux appears to decline more rapidly, and in our last binned observation is significantly below our fitted model. This appears to provide evidence for an additional break at  $\sim 2 \times 10^6$  s, but beyond this point the afterglow flux faded below the XRT detection threshold and further observations are unavailable, so we cannot independently verify this behavior.

As discussed previously in §2.7, the X-ray spectrum appears invariant over the entire burst evolution within fairly stringent constraints. At early times (during the smooth early decay) we measure  $\beta_{X,1} = 0.814 \pm 0.013$ ; during the late phase we measure  $\beta_{X,2} = 0.80 \pm 0.04$ .

### 3.4. Testing Canonical Models

We are able to measure  $\alpha$  and  $\beta$  very precisely throughout most of the evolution of the light curve in both optical and X-ray bands (limited in most cases only by the assumptions

of the model itself, e.g., the possible presence of additional underlying components, rather than the actual statistical uncertainty). In principle this should allow us a strong test of the canonical fireball model (e.g., Sari et al. 1998).

During the rapid decay phase of the afterglow, we measure (after extinction correction)  $\alpha_{\text{opt}} = 2.2$ ,  $\beta_{\text{opt}} = 0.5$  in the UV-optical-IR range (though both values are somewhat variable). Unsurprisingly, this combination of large  $\alpha$  and low  $\beta$  is not well-fit by any canonical forward-shock model (e.g., Price et al. 2003), with the exception of a jet model where  $\nu_{\text{opt}} < \nu_c$ , which is approximately consistent with both values for  $p = 2.0 - 2.2$ . We will return to the possibility of an extremely early jet break in §3.6, but the later evolution of the light curve (in which it flattens) casts doubt on this interpretation. Alternatively, the reverse-shock model (Kobayashi 2000) also predicts a very steep early decay, although even this model cannot exactly reconcile the steep decay with the observed spectral index; given  $\alpha = 2.2$  this model predicts  $\beta=0.8$ . Still, this is a significant improvement over any forward-shock model. A third possibility, favored by Kumar & Panaitescu (2008), is that the early steep decay is actually “high latitude” emission: prompt emission whose arrival at the observer was delayed because it is slightly off-axis. In this case a value of  $\beta = \alpha - 2 = 0.2$  is predicted, which is also not consistent with our observations. In fact, the observed value is nearly exactly between the reverse-shock and high-latitude values. It is possible that both models may contribute in about equal degrees to the observations and produce an intermediate spectral index (which may also explain some of the small-scale variation in the observed  $\alpha$ ).

At about the same time when the optical light curve is rapidly decaying, the X-ray light curve is relatively flat, with  $\alpha_X = 1.48$ . Comparing the relative optical and X-ray fluxes, the optical flux overpredicts the X-ray flux at early times; the optical and X-ray bands also have different spectral indices, suggesting that a spectral break is present between the two bands and that this break is moving upward in frequency with time. Given the disparate behavior from the contemporaneous optical light curve and the shift to different behavior at late time, the early X-ray emission appears to come from a different origin or process as the rest of the light curve; we do not attempt to explain it within the standard model.

Once the optical light curve begins to level out (in the transition zone between the early and late-time components), the spectral index evolves to surprisingly blue values. An average SED formed from data points during the extremely well-observed region, using observations from  $K$  through the UV between 5500 and 12,000 s, constrains the average SED to  $\beta_{\text{opt}} = 0.07 \pm 0.03$  (see also Figure 5). It is impossible to generate  $\beta < 0.5$  during a declining light curve within the basic synchrotron model, so this offers strong corroborating evidence that the underlying component responsible for the majority of the optical flux is

undergoing a break at this time. The canonical model (Sari et al. 1998) could naturally explain this portion of the light curve as a characteristic-frequency peak, when  $\nu_m$  crosses through the UV, optical, and IR bands (in that order), causing a gradual shift in the overall color from  $\beta = -1/3$  to  $\beta = (p - 1)/2$ . It is in fact difficult to explain this feature in any other straightforward way; in a wind medium the same feature shifts in color only from  $\beta = 1/2$  to  $\beta = p/2$  (Li & Chevalier 2003) which is never sufficiently blue. Complicated prescriptions involving numerous components contributing about equally to the afterglow flux (e.g., Racusin et al. 2008b) may also explain this feature, though at the expense of substantial additional complexity.

Although the optical SED provides good evidence of shifting somewhat back toward the red at late times, its overall blueness remains a challenge to explain even after a simple power-law decay has set in. This late decay rate is  $\alpha_{\text{opt}} = 1.23 \pm 0.02$  optically, and  $\alpha_X = 1.30 \pm 0.05$  in X-rays. Fitting to a combination of the first three epochs of the late-time Gemini data gives  $\beta_{\text{opt}} = 0.51 \pm 0.26$ . If we assume that the X-ray and optical afterglows have the same origin, then the X-ray to optical spectral index is  $\beta_{\text{OX}} = 0.77 \pm 0.01$  — consistent with the X-ray index itself of  $\beta_X = 0.80 \pm 0.04$ . This also forms a strict upper limit on  $\beta_{\text{opt}}$ ; even if a cooling break is present close to the optical band (our observations do not rule out this possibility) then  $\beta_{\text{opt}} < \beta_{\text{OX}}$  to not underpredict the X-ray flux.

Given this, and assuming  $p \geq 2$ , we can greatly constrain the available models. The jet model (which we favored in the first version of this paper, before late-time data were available) is completely ruled out (it requires  $\alpha \geq 2.0$ ), as are models where the optical band is above the cooling break (which requires  $\beta \geq 1.0$ ). This leaves only two possibilities. The interstellar medium (ISM) model discussed previously is, in principle, still in agreement (barely) with the data: for  $p = 2.59$ ,  $\alpha = 1.19$  and  $\beta = 0.79$ , all within  $2\sigma$  of observed values. However this requires that the X-ray regime also be below the cooling frequency ( $\nu_X < \nu_c$ ) out to extremely late times (at least 10 d), which is not expected physically in the ISM model unless the density  $n$  and/or the magnetization fraction  $\epsilon_B$  are very low:

$$\left(\frac{n}{\text{cm}^{-3}}\right) \left(\frac{\epsilon_B}{4 \times 10^{-5}}\right)^{3/2} \lesssim 1.$$

Alternatively, a wind model with  $p = 2.0$  predicts  $\alpha_{\text{opt}} = 1.25$  and  $\beta_{\text{opt}} = 0.50$ . These are reasonable, but the X-ray flux is either greatly over-predicted (if a cooling break is absent, we would anticipate  $\beta_{\text{OX}} = 0.50$  as well), or the X-ray decay is far too fast (if a cooling break is present, then  $\alpha_X = 1.0$ ). Either possibility is ruled out to at least  $6\sigma$ .

We therefore prefer the ISM model to favor all observations. While a wind-stratified medium may be made to work with sufficient enhancements (for example, the chromatic optical behavior could be explained by an additional emission component, and the late-

time discrepancies in the optical and X-rays could be explained by evolution of the cooling frequency in a way not predicted by canonical models), this model is simpler as it explains all of our observations without the need for such components — with the exception of the very early-time data, where standard assumptions are most expected not to hold. Our conclusion here therefore disagrees with that of Kumar & Panaitescu (2008) and Racusin et al. (2008b), who prefer a wind-stratified model at late times.

### 3.5. Frequency Domain Searches

Given the brightness of the event, we analyzed the high time cadence  $\gamma$ -ray, X-ray, and IR data in search of any significant trends in the frequency domain. The power-density spectrum (PDS) for the *INTEGRAL* data (Beckmann et al. 2008), spanning  $f = 0.03$  to 5 Hz, is well fit by a power law with  $P(f)df \propto f^{-1.8}$ . This index here is consistent with the  $-5/3$  reported for a number of bright GRBs (Beloborodov et al. 1998; Chang & Yi 2000), and is interpreted as evidence for fully developed turbulence. The PDS from the *Swift* XRT data is essentially (white) noise, apart from  $1/f$  noise at short frequencies. An analysis of the first  $\sim 2$  hr of PAIRITEL *J*-band photometry also shows a featureless PDS aside from  $1/f$  noise.

### 3.6. Energetics

The emission from GRB 080319B makes it one of the most energetic GRBs ever detected and the most energetic thus far seen by *Swift*. A preliminary analysis of Konus-Wind observations reported by Golenetskii et al. (2008) yields a burst fluence of  $5.72_{-0.13}^{+0.14} \times 10^{-4}$  erg  $\text{cm}^{-2}$  in a 20 keV to 7 MeV energy window. This corresponds to a fluence of  $5.31 \times 10^{-4}$  erg  $\text{cm}^{-2}$  in the BATSE bandpass of 20 keV to 1.8 MeV, making it brighter than the highest-fluence BATSE burst ( $4.08 \times 10^{-4}$  erg  $\text{cm}^{-2}$ ; Kaneko et al. 2006). The rest-frame isotropic equivalent energy release is  $E_{\text{iso}} = 1.3 \times 10^{54}$  erg in the standard source frame  $1 - 10^4$  keV band (Amati et al. 2002; Bloom et al. 2001).

If the true collimation-corrected energy ( $E_\gamma$ ) of GRB080319B is comparable to the median value of  $E_\gamma = 1.33 \times 10^{51}$  erg found by Bloom et al. (2003), and if we assume average values for the efficiency of converting the blast wave’s kinetic energy into gamma rays of  $\eta_\gamma = 0.5$  and the circumburst density  $n = 1.0 \text{ cm}^{-3}$  (Granot & Kumar 2006; Kumar et al. 2007), then a jet break is expected at  $3.6 \times 10^4$  s post trigger. A circumburst density greater than  $n = 1 \text{ cm}^{-3}$  only hastens the predicted light-curve break, with  $n = 100 \text{ cm}^{-3}$  resulting

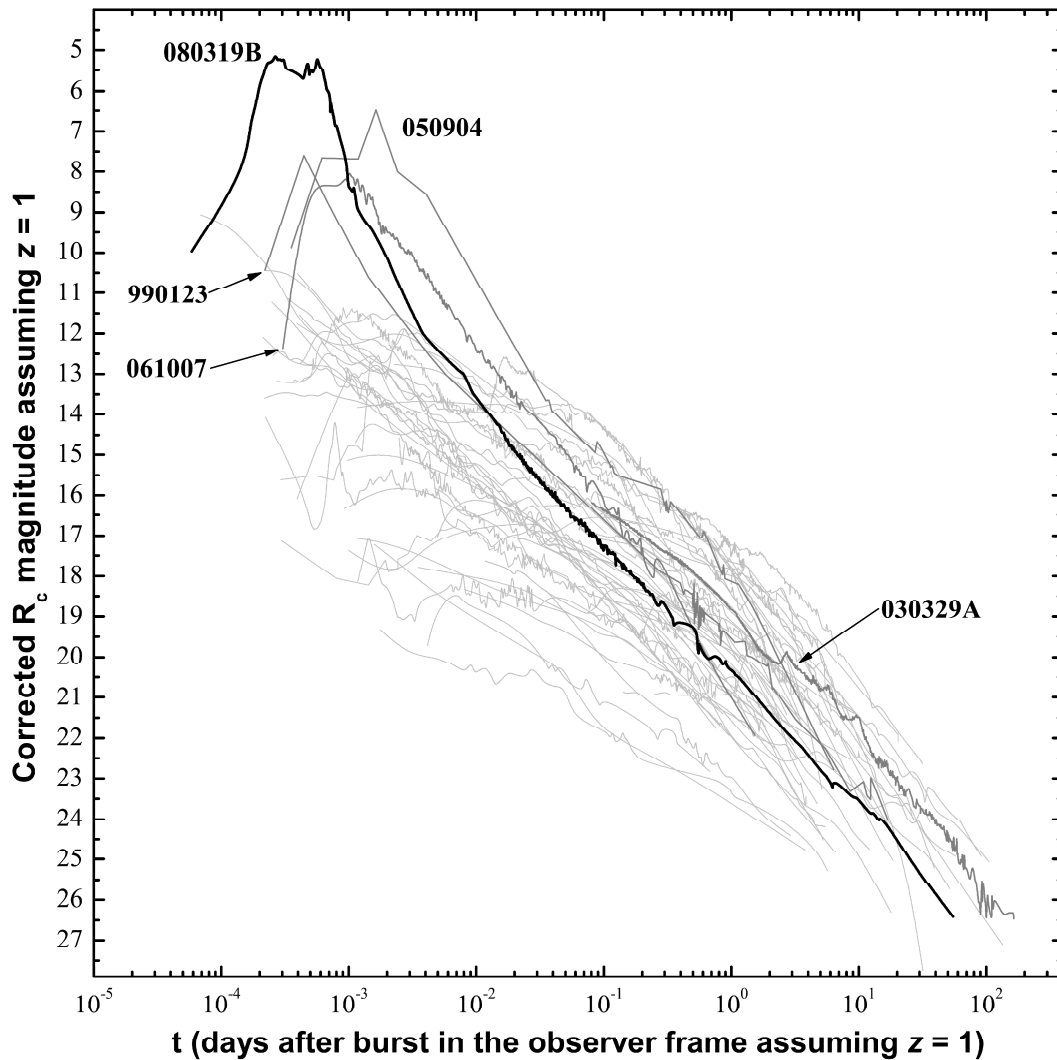


Fig. 7.— Comparison between the observed  $R$ -band light curve of GRB 080319B and those of other GRB afterglows, both from the pre-*Swift* as well as the *Swift* era, shifted to a common redshift of  $z = 1$  with the method of Kann et al. (2006). The prompt flash of GRB 080319B is clearly shown to be the most luminous optical transient ever observed with a high degree of confidence. In spite of this, because of its rapid early decay the afterglow at late times is quite unremarkable, and is similar in this regard to the three other “ultra-luminous” bursts to date: GRBs 990123, 061007, and 050904. In contrast, the bursts that remain the brightest tend to be those with late plateaus and slow decays.

in  $t_{\text{jet}} = 7.8 \times 10^3$  s. Likewise, a collimation-corrected energy less than  $E_\gamma = 1.3 \times 10^{51}$  erg will also push the expected jet break to earlier times, with  $E_\gamma = 10^{50}$  erg yielding  $t_{\text{jet}} \approx 10^3$  s.

No canonical jet break is observed in the GRB light curve. The only unambiguous steepening feature is an X-ray break observed at  $t = 2620 \pm 470$  s. However, no contemporaneous optical break is observed. There is evidence of a break at very late times ( $\gtrsim 10^6$  s). Unfortunately, the afterglow is extremely faint at this point, but both the last X-ray observation, the last *g*-band detection, and the final *HST F606W* measurement from the GCN circulars are significantly (though only mildly:  $2\text{--}3\sigma$ ) below our fitted power-law extrapolation. Furthermore, the fact that the afterglow shifts to dramatically redder colors at this point (simultaneously,  $i$  and  $z$  rise above the fitted curve) suggests that the optical flux may be dominated by supernova light (§3.7; host-galaxy light likely contributes as well), and the afterglow contribution is actually even smaller than this, which would strongly favor a break. Unfortunately, given the lack of available late-time X-ray data we cannot strongly constrain whether or not the break is chromatic.

Treating this feature as a jet break, the very late break time ( $t = 10$  d) imposes strong demands on the afterglow energetics. Assuming  $n = 1 \text{ cm}^{-3}$  and  $\eta_\gamma = 0.5$ , this places a lower limit on the collimation-corrected energy of  $4.0 \times 10^{51}$  erg, significantly higher than any pre-*Swift* value (Bloom et al. 2003) and the vast majority of *Swift* bursts, but comparable to the handful of “hyper-energetic” outlier events discovered by *Swift*: GRBs 050904 (Tagliaferri et al. 2005), 050820A (Cenko et al. 2006), and 070125 (Chandra et al. 2008; Utdike et al. 2008). The lack of an early jet break would then argue that the extreme brightness of this GRB is at least partially intrinsic to the explosion itself.

Alternatively, a jet break may have occurred extremely early (within the first 100 s) before the start of our observations. Such a model has been suggested to explain the lack of an apparent jet break in another powerful event detected by *Swift*, such as GRB 061007 — see Schady et al. 2007a and Mundell et al. 2007). In this case,  $E_\gamma$  would actually have an unusually *low*, though not unprecedented, energy release of  $\sim 10^{49}$  erg. One could also appeal to the minor break in the X-ray light curve (and presume the optical break was hidden by other effects), which would indicate a fairly canonical energy near  $10^{51}$  erg; either of these cases would point to extreme collimation given the large  $E_{\text{iso}}$ . However, as we have already discussed, in these cases the “post-break” light-curve slopes in the optical and X-rays of  $\alpha_O = 1.23$  and  $\alpha_X = 1.40$  are much too shallow for the prediction of  $t^{-p}$  (Sari et al. 1999), where generally we expect the electron index  $p \geq 2.0$ .

A final possibility is that multiple jets, with very different opening angles, were involved, similar to the model proposed for GRB 030329 (Berger et al. 2003). In this scenario, we might expect to see both an early break (from highly collimated, highly relativistic emission)

and a late break (from less collimated, less relativistic emission), presuming that the emission at different times was dominated by different jet components. Assuming that the prompt emission and optical flash were associated with the narrow jet, the lack of a break at late times<sup>5</sup> need not imply unusual energetics. The fact that the early-time X-ray break is very sharp, and also apparently achromatic, might argue for this interpretation, and the lack of a contemporaneous optical break could be explained if the optical counterpart of the early X-ray shallow decay phase were hidden by the bright reverse shock. This model is the one favored by Racusin et al. (2008b).

### 3.7. Supernova Constraints

Detailing the nature of the late-time behavior and the evolution of the likely supernova counterpart is beyond the scope of this paper, but we performed a few basic fits using the method of Zeh et al. (2004) of the late-times observations under various model assumptions (host brightnesses, using an extrapolation of the late-time light curve and a SN 1998bw-like supernova template). In all assumptions we measure a luminosity relative to SN 1998bw in the same rest-frame epoch, of greater than one, with an overall distribution of  $k = 2.3 \pm 0.8$  (Figure 6). In particular, the existence of a late afterglow break and host galaxy with a magnitude comparable to the HST measurement of Levan et al. (2008) favor higher values, which provides evidence that this unusually bright GRB may be associated with an unusually bright (even compared to other GRB supernovae: Ferrero et al. 2006) supernova. For  $s$ , the relative rest-frame time to maximum light relative to SN 1998bw, we measure  $s = 0.89 \pm 0.10$ .

## 4. Discussion and Conclusions

The PDS analysis reflects quantitatively what is qualitatively a light curve without strong brightening features. Such “smooth” afterglows have been seen before (e.g., Laursen & Stanek 2003; Stanek et al. 2005), yet many GRBs with high-quality optical/IR afterglow observations show significant jaggedness, often on timescales less than the time since trigger (e.g., Jakobsson et al. 2004). The afterglow in this case is not entirely featureless; slow modulations of less than 10% with  $\Delta t/t$  are observed at around 200 s and 700 s, but these have been seen before in other afterglows, including the undulating afterglow of GRB 030329

---

<sup>5</sup>To be sure, Racusin et al. (2008b) claim a late-time jet break but we find no significant evidence of such in the XRT data alone. The apparent discrepancy may be due to the different time binnings of the late-time data.

(Lipkin et al. 2004).

While an observation of periodicity ( $f \gtrsim 1$  Hz) in the prompt phase could be considered a reasonable manifestation of a magnetized neutron star powering the initial internal shocks (e.g., Metzger et al. 2008), the absence of such a signature in the *INTEGRAL* PDS by no means rules out such a hypothesis. The concordance of the PDS with other GRBs in the pre-*Swift* sample suggests, *prima facie*, a similarity between GRB 080319B and other events in the hydrodynamic properties of the (emitting) outflow; also absent is any substantial evidence for a difference in microphysical parameters. We are left with the reasonable conclusion that the extreme brightness of GRB 080319B has more to do with macroscopic parameters of the central engine (in particular, the collimation angle,  $M_{\text{ejecta}}$ , initial Lorentz factor, and possibly the circumburst medium could all be responsible) than extrema in shock parameters.

There is a qualitative similarity in the intrinsic behavior of the three brightest afterglow events (Fig. 7), requiring more than 9 s in the rest frame from  $\gamma$ -ray trigger to reach peak brightness. Yet, as noted with GRBs 050904 and 990123 (Kann et al. 2007a), even the brightest events fade very rapidly and reach by day 1 a magnitude comparable to that of the general population. In our adopted cosmology,  $M_{\text{peak},r} = -38.3$  mag at a time  $t \approx 10$  s (rest frame) from trigger. Likewise,  $M_{\text{peak},r}(990123) = -36.0$  mag at a time  $t = 18.1$  s and  $M_{\text{peak},r}(050904) = -37.1$  mag at a time  $t = 71.2$  s. Compared to GRBs 990123 and 050904, GRB 080319B does not appear to support the proposed brightness vs.  $t_{\text{peak}}$  relation (Panaitescu & Vestrand 2008) (i.e., that brighter events are seen to take longer from trigger to peak); still, the existence of a rough relation when including fainter events suggests that the very brightest events such as these may allow for the longest follow-up delay at a given redshift. This afterglow “turn on” delay for some fraction of events has important implications for follow-up of high-redshift GRBs since tens of seconds in the rest frame becomes a delay of minutes in the observer frame (Fig. 9). Such a consideration, for example, could relax requirements for extremely rapid repointing of satellites to catch afterglows at their brightest.

Figure 8 shows the comparison between GRB 080319B, quasars, and one of the most energetic supernova recorded (SN 2006gy; Smith et al. 2007). While evolutionary effects in all three populations are sure to be important at some level (with QSOs fainter at higher redshift, etc.), in the context of probing the high-redshift universe, the overall impression is clear: for  $\sim 30$  min in the rest frame (what would be  $\sim 4$  hr in the observer frame at  $z = 7$ ), GRB 080319b would have been brighter than the brightest known QSO in the universe (see also Lazzati et al. 2001; Kann et al. 2006 for a discussion comparison of the GRB population with QSOs).

We now turn our attention to *detectability* of such GRBs at high redshift (leaving aside



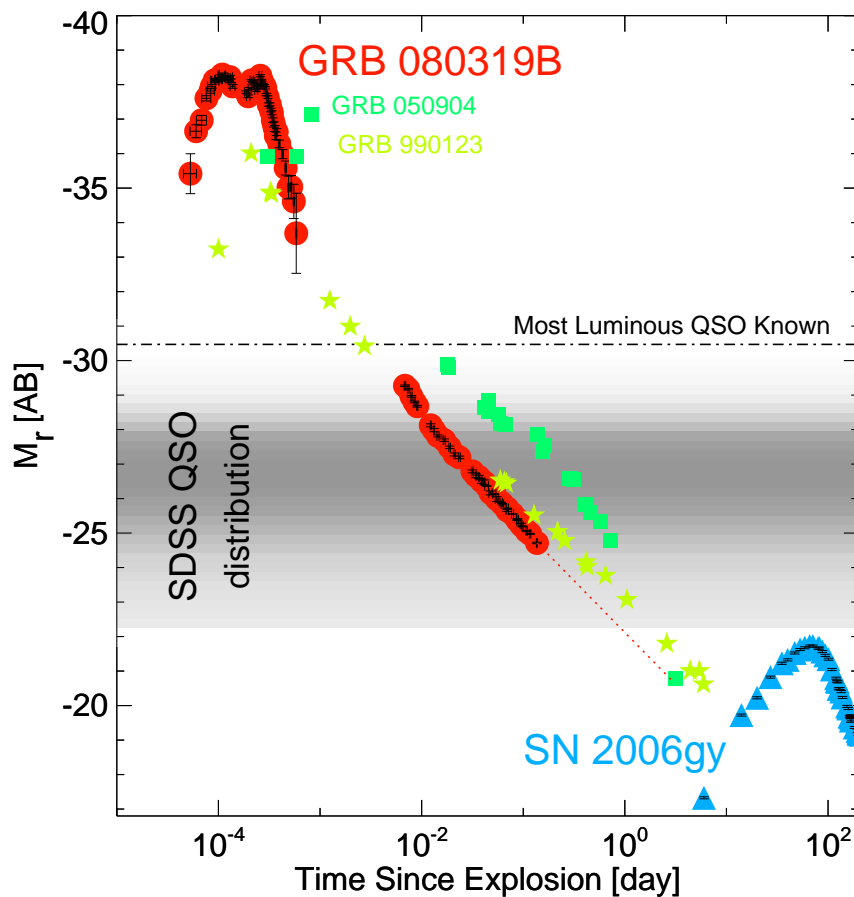


Fig. 8.— Rest-frame comparison of the most luminous optical/IR probes of the distant universe, showing the absolute magnitude ( $M_r$ , in AB magnitudes as defined by Oke & Gunn 1982) versus time of GRB 080319B (red circles) and SN 2006gy (blue triangles; Smith et al. 2007). Transformed light curves of GRB 990123 (yellow stars; adapted from Galama et al. 1999) and GRB 050904 (green squares; adapted from Kann et al. 2007b) are also shown. For reference, the most luminous known QSO (Schneider et al. 2007) is shown with a dashed horizontal line; the distribution of SDSS QSO magnitudes, adapted from Fig. 6 of Schneider et al., is shown as horizontal banding (darker indicates higher density of sources per unit magnitude). The afterglow of GRB 080319B was the brightest GRB afterglow ever recorded and was at early times  $\sim 10^3$  times more luminous than the most luminous QSO.

the question of their *existence*; see, e.g., Bromm & Loeb 2007; Naoz & Bromberg 2007). Given the observed light curve and intrinsic spectrum of this burst (§ 2), to what redshift could similar events be detected by present and future missions? The peak photon flux from GRB 080319B in 1 s is  $\sim 1 \times 10^{59}$  photons  $\text{s}^{-1}$ . For a BAT threshold flux of 0.8 photons  $\text{cm}^{-2} \text{s}^{-1}$  for  $E_{\text{pk,obs}} \gtrsim 100$  keV (Band 2003), the event would be detected out to  $z = 10.7$  ( $8\sigma$ ). For the nominal EXIST (Grindlay 2007) threshold of 0.2 photons  $\text{cm}^{-2} \text{s}^{-1}$ , the event would be detected out to  $z = 32$ . The ability to detect an afterglow for an extreme event of this nature is even more remarkable because of time-dilation effects — shifted to  $z \approx 32$  or potentially even further, the afterglow luminosity at late times is nearly independent of distance at high redshift. Aside from the effects of line-of-sight absorption by neutral hydrogen, GRB 080319B would remain visible even if placed well into the epoch of reionization (Fig. 9).

We conclude with a rumination on the extrapolation of the features of the afterglow toward the low-redshift universe. At  $z = 0.17$ , the distance of the nearest non-underluminous GRB to date (GRB 030329), this event would peak at  $R \approx 1$  mag, nearly as bright as the brightest stars in the sky. Or, to carry the comparison to its greatest extreme, we might envision a situation in which a GRB similar to GRB 080319B were to occur in our own Galaxy. At a distance of 1 kpc (and neglecting the probable substantial extinction along Galactic lines of sight at optical wavelengths), the optical flash would peak at magnitude about  $-28.5$ , several times the brightness of the Sun! Such an event must assuredly be extremely unusual — the Galactic GRB rate is probably no greater than 1 per  $10^5$  to  $10^6$  years (Podsiadlowski et al. 2004; see also Stanek et al. 2006), likely only 1% of such bursts are collimated toward Earth, and this is among the brightest 0.1% of bursts ever observed. Altogether, the rate is probably less than 1 per  $10^{10} - 10^{11}$  yr: unlikely to have ever happened even over the long timescale of geological history, and certainly not a spectacle we can expect to witness anytime soon.

Much of this research could not have been undertaken without the work of S. Barthelmy running the GCN Circulares and the *Swift* team for their extraordinary efforts. N.R.B. was partially supported by a SciDAC grant from the Department of Energy. J.S.B., J.X.P., and H.-W.C. are partially supported by NASA/*Swift* grant #NNG05GF55G. A.V.F.’s group at U.C. Berkeley is supported by National Science Foundation (NSF) grant AST-0607485 and the TABASGO Foundation, as well as by NASA/*Swift* Guest Investigator grants #NNG05GF35G and #NNG06GI86G. S.L. was partly supported by the Chilean *Centro de Astrofísica* FON-DAP No. 15010003 and by FONDECYT grant N°1060823. We thank J. Brewer of the IFMD Foundation. This publication makes use of data products from the Two Micron All Sky Survey, which is a joint project of the University of Massachusetts and the Infrared

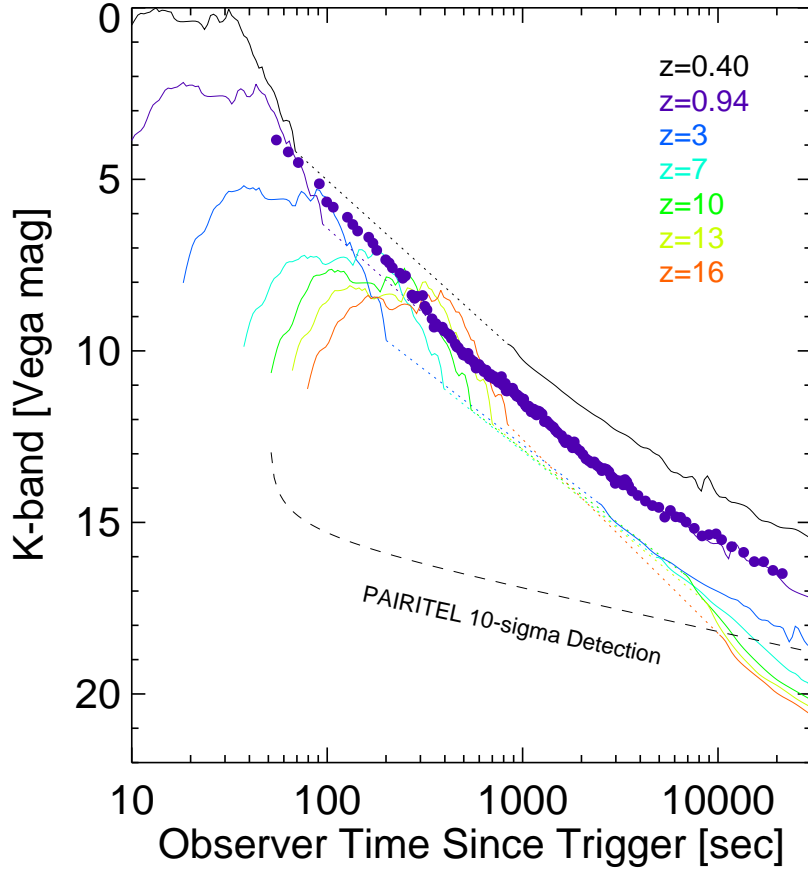


Fig. 9.— Observability of GRB 080319B in observer-frame  $K$  band at a variety of redshifts, based on a simple model of the temporal and spectral evolution of the afterglow bootstrapped from the  $V$ -band light curve. Dotted lines cover the gap in optical ( $V$ -band) coverage. The afterglow, which would have been as bright as Vega if the event occurred at  $z = 0.40$ , remains remarkably bright even to  $z \approx 16$ . The purple filled circles show the observed  $K$ -band light curve from this paper, showing a good agreement with the model of the  $z = 0.937$  (purple) curve (suggesting, too, that the interpolation in the  $V$ -band time gap is appropriate). The PAIRITEL cumulative  $10\sigma$  point-source sensitivity is shown, assuming a nominal start time after GRB trigger of 51 s. For all redshifts where the Universe is transparent to  $\text{Ly}\alpha$  photons, this source could have easily been detected by sub-meter class telescopes.

Processing and Analysis Center/California Institute of Technology, funded by NASA and the NSF. KAIT and its ongoing research were made possible by donations from Sun Microsystems, Inc., the Hewlett-Packard Company, AutoScope Corporation, Lick Observatory, the NSF, the University of California, the Sylvia & Jim Katzman Foundation, and the TABASGO Foundation. Partially, based on observations obtained at the Gemini Observatory, which is operated by the Association of Universities for Research in Astronomy, Inc., under a cooperative agreement with the NSF on behalf of the Gemini partnership: the National Science Foundation (United States), the Science and Technology Facilities Council (United Kingdom), the National Research Council (Canada), CONICYT (Chile), the Australian Research Council (Australia), Ministrio da Cincia e Tecnologia (Brazil) and SECYT (Argentina). We thank the Gemini Observatory staff for their excellent work in observing GRB 080319B; the assistance of the Lick Observatory staff is also acknowledged. The Peters Automated Infrared Imaging Telescope is operated by the Smithsonian Astrophysical Observatory (SAO) and was made possible by a grant from the Harvard University Milton Fund, the camera loan from the University of Virginia, and the continued support of the SAO and UC Berkeley. The PAIRITEL project is further supported by NASA/Swift Guest Investigator Grant #NNG06GH50G. We are grateful to E. E. Falco and the Mt. Hopkins staff (W. Peters, R. Hutchins, T. Groner) for their continued assistance with PAIRITEL.

## REFERENCES

- Adelman-McCarthy, J. K. *et al.* 2008, *ApJS*, 175, 297
- Amati, L. *et al.* 2002, *A&A*, 390, 81
- Band, D. L. 2003, *ApJ*, 588, 945
- Beckmann, V., Mereghetti, S., Kienlin, A. v., Beck, M., Savchenko, V., Borkowski, J., and Gotz, D. 2008, *GCN Circular* 7450
- Beloborodov, A. M., Stern, B. E., and Svensson, R. 1998, *ApJ*, 508, L25
- Berger, E. *et al.* 2003, *Nature*, 426, 154
- Bertin, E. and Arnouts, S. 1996, *A&AS*, 117, 393
- Beuermann, K. *et al.* 1999, *A&A*, 352, L26
- Bloom, J. S., Frail, D. A., and Kulkarni, S. R. 2003, *ApJ*, 594, 674
- Bloom, J. S., Frail, D. A., and Sari, R. 2001, *AJ*, 121, 2879

- Bloom, J. S., Starr, D., and Perley, D. A. 2008, GCN Circular 7434
- Bloom, J. S., Starr, D. L., Blake, C. H., Skrutskie, M. F., and Falco, E. E. 2006, in *Astronomical Society of the Pacific Conference Series*, Vol. 351, *Astronomical Data Analysis Software and Systems XV*, ed. C. Gabriel, C. Arviset, D. Ponz, & S. Enrique, 751
- Bromm, V. and Loeb, A. 2007, in *American Institute of Physics Conference Series*, Vol. 937, *Supernova 1987A: 20 Years After: Supernovae and Gamma-Ray Bursters*, ed. S. Immler, K. Weiler, & R. McCray, 532–541
- Butler, N. 2008, GCN Circular 7499
- Butler, N. R. and Kocevski, D. 2007a, *ApJ*, 663, 407
- . 2007b, *ApJ*, 668, 400
- Butler, N. R., Kocevski, D., Bloom, J. S., and Curtis, J. L. 2007, *ApJ*, 671, 656
- Cenko, S. B. *et al.* 2006, *ApJ*, 652, 490
- Chandra, P. *et al.* 2008, ArXiv e-prints, 0802.2748
- Chang, H.-Y. and Yi, I. 2000, *ApJ*, 542, L17
- Cool, R. J. *et al.* 2008, GCN Circular 7465
- Covino, S. *et al.* 2008, GCN Circular 7446
- Cwiok, M. *et al.* 2008a, GCN Circular 7445
- . 2008b, GCN Circular 7445
- Daigne, F., Rossi, E. M., and Mochkovitch, R. 2006, *MNRAS*, 372, 1034
- Eisner, J. A., Hillenbrand, L. A., White, R. J., Bloom, J. S., Akeson, R. L., and Blake, C. H. 2007, *ApJ*, 669, 1072
- Ferrero, P. *et al.* 2006, *A&A*, 457, 857
- Filippenko, A. V., Li, W. D., Treffers, R. R., and Modjaz, M. 2001, in *Astronomical Society of the Pacific Conference Series*, Vol. 246, *IAU Colloq. 183: Small Telescope Astronomy on Global Scales*, ed. B. Paczynski, W.-P. Chen, & C. Lemme (San Francisco, CA: ASP), 121
- Foley, R. J. *et al.* 2006, *ApJ*, 645, 450

- Galama, T. J. *et al.* 1999, *Nature*, 398, 394
- Gehrels, N. *et al.* 2004, *ApJ*, 611, 1005
- Giblin, T. W., van Paradijs, J., Kouveliotou, C., Connaughton, V., Wijers, R. A. M. J., Briggs, M. S., Preece, R. D., and Fishman, G. J. 1999, *ApJ*, 524, L47
- Golenetskii, S., Aptekar, R., Mazets, E., Pal’shin, V., Frederiks, D., and Cline, T. 2008, GCN Circular 7482
- Granot, J. and Kumar, P. 2006, *MNRAS*, 366, L13
- Grindlay, J. E. 2007, in *American Institute of Physics Conference Series*, Vol. 921, *The First GLAST Symposium*, ed. S. Ritz, P. Michelson, & C. A. Meegan (New York, NY: AIP), 211–216
- Henden, A. 2008, GCN Circular 7528
- Hentunen, V., Oksanen, A., and Kehusmaa, P. 2008, GCN Circular 7484
- Hook, I. M., Jørgensen, I., Allington-Smith, J. R., Davies, R. L., Metcalfe, N., Murowinski, R. G., and Crampton, D. 2004, *PASP*, 116, 425
- Horne, K. 1986, *PASP*, 98, 609
- Jakobsson, P. *et al.* 2004, *New Astronomy*, 9, 435
- . 2006, *A&A*, 447, 897
- Jelinek, M., Castro-Tirado, A. J., Chantry, V., and Plá, J. 2008, GCN Circular 7476
- Kaneko, Y., Preece, R. D., Briggs, M. S., Paciesas, W. S., Meegan, C. A., and Band, D. L. 2006, *ApJS*, 166, 298
- Kann, D. A., Klose, S., and Zeh, A. 2006, *ApJ*, 641, 993
- Kann, D. A. *et al.* 2007a, *ArXiv e-prints*, 0712.2186
- Kann, D. A., Masetti, N., and Klose, S. 2007b, *AJ*, 133, 1187
- Karpov, S. *et al.* 2008a, GCN Circular 7452
- . 2008b, GCN Circular 7558
- Kobayashi, S. 2000, *ApJ*, 545, 807

- Krugly, Y., Slyusarev, I., and Pozanenko, A. 2008, GCN Circular 7519
- Kumar, P. *et al.* 2007, MNRAS, 376, L57
- Kumar, P. and Panaitescu, A. 2008, ArXiv e-prints, 0805.0144
- Laursen, L. T. and Stanek, K. Z. 2003, ApJ, 597, L107
- Lazzati, D., Ghisellini, G., Haardt, F., and Fernández-Soto, A. 2001, in Gamma-ray Bursts in the Afterglow Era, ed. E. Costa, F. Frontera, & J. Hjorth, 191
- Le, T. and Dermer, C. D. 2007, ApJ, 661, 394
- Levan, A. J., Tanvir, N. R., Fruchter, A. S., and Graham, J. 2008, GCN Circular 7710
- Li, W., Chornock, R., Perley, D. A., and Filippenko, A. V. 2008, GCN Circular 7438
- Li, W., Filippenko, A. V., Chornock, R., and Jha, S. 2003, PASP, 115, 844
- Li, W., Jha, S., Filippenko, A. V., Bloom, J. S., Pooley, D., Foley, R. J., and Perley, D. A. 2006, PASP, 118, 37
- Li, Z.-Y. and Chevalier, R. A. 2003, in Lecture Notes in Physics, Berlin Springer Verlag, Vol. 598, Supernovae and Gamma-Ray Bursters, ed. K. Weiler, 419–444
- Lipkin, Y. M. *et al.* 2004, ApJ, 606, 381
- Metzger, B. D., Thompson, T. A., and Quataert, E. 2008, ApJ, 676, 1130
- Mundell, C. G. *et al.* 2007, ApJ, 660, 489
- Naoz, S. and Bromberg, O. 2007, MNRAS, 380, 757
- Novak, R. 2008, GCN Circular 7504
- Oke, J. B. and Gunn, J. E. 1982, PASP, 94, 586
- Panaitescu, A. and Vestrand, W. T. 2008, MNRAS, 387, 497
- Perley, D. A. *et al.* 2008, ApJ, 672, 449
- Podsiadlowski, P., Mazzali, P. A., Nomoto, K., Lazzati, D., and Cappellaro, E. 2004, ApJ, 607, L17
- Poole, T. S. *et al.* 2008, MNRAS, 383, 627

- Price, P. A. *et al.* 2003, *ApJ*, 589, 838
- Racusin, J. L., Gehrels, N., Holland, S. T., Kennea, J. A., Markwardt, C. B., Pagani, C., Palmer, D. M., and Stamatikos, M. 2008a, GCN Circular 7427
- Racusin, J. L. *et al.* 2008b, ArXiv e-prints, 0805.1557
- Sari, R., Piran, T., and Halpern, J. P. 1999, *ApJ*, 519, L17
- Sari, R., Piran, T., and Narayan, R. 1998, *ApJ*, 497, L17+
- Schady, P. *et al.* 2007a, *MNRAS*, 380, 1041
- . 2007b, *MNRAS*, 377, 273
- Schlegel, D. J., Finkbeiner, D. P., and Davis, M. 1998, *ApJ*, 500, 525
- Schneider, D. P. *et al.* 2007, *AJ*, 134, 102
- Schubel, M. *et al.* 2008, GCN Circular 7461
- Smith, N. *et al.* 2007, *ApJ*, 666, 1116
- Stanek, K. Z. *et al.* 2005, *ApJ*, 626, L5
- . 2006, *Acta Astronomica*, 56, 333
- Swan, H., Yuan, F., and Rujopakarn, W. 2008, GCN Circular 7470
- Tagliaferri, G. *et al.* 2005, *A&A*, 443, L1
- Tanvir, N. R., Levan, A. J., Fruchter, A. S., Graham, J., Wiersema, K., and Rol, E. 2008, GCN Circular 7569
- Updike, A. C. *et al.* 2008, ArXiv e-prints, 0805.1094
- Vreeswijk, P. M., Smette, A., Malesani, D., Fynbo, J. P. U., Milvang-Jensen, B., Jakobsson, P., Jaunsen, A. O., and Ledoux, C. 2008, GCN Circular 7444
- Wood-Vasey, W. M. *et al.* 2007, ArXiv e-prints, 0711.2068
- Wozniak, P., Vestrand, W. T., Wren, J., and Davis, H. 2008, GCN Circular 7464
- Zeh, A., Klose, S., and Hartmann, D. H. 2004, *ApJ*, 609, 952



Table 1. PAIRITEL Observations of GRB 080319B

$t_{\text{mid}}^{\text{a}}$ sec	Filter	Exp. time sec	Mag. <sup>b</sup>	Flux <sup>b</sup> $\mu\text{Jy}$
344.0	J	7.8	$10.389 \pm 0.048$	$111255.0 \pm 4815.5$
352.3	J	7.8	$10.483 \pm 0.048$	$102084.5 \pm 4419.0$
360.2	J	7.8	$10.563 \pm 0.048$	$94763.2 \pm 4102.4$
380.1	J	7.8	$10.652 \pm 0.048$	$87313.1 \pm 3779.8$
388.4	J	7.8	$10.722 \pm 0.048$	$81846.4 \pm 3544.3$
396.3	J	7.8	$10.781 \pm 0.048$	$77538.9 \pm 3357.8$
416.3	J	7.8	$10.877 \pm 0.048$	$70983.9 \pm 3074.6$
424.5	J	7.8	$10.896 \pm 0.048$	$69752.5 \pm 3021.6$
432.4	J	7.8	$10.952 \pm 0.048$	$66227.7 \pm 2868.9$
344.0	H	7.8	$9.639 \pm 0.042$	$142696.2 \pm 5421.2$
352.3	H	7.8	$9.721 \pm 0.042$	$132364.7 \pm 5029.4$
360.2	H	7.8	$9.753 \pm 0.042$	$128513.3 \pm 4883.6$
380.1	H	7.8	$9.946 \pm 0.042$	$107582.1 \pm 4088.8$
388.4	H	7.8	$9.985 \pm 0.042$	$103750.1 \pm 3944.2$
396.3	H	7.8	$10.115 \pm 0.042$	$92078.9 \pm 3501.5$
416.3	H	7.8	$10.127 \pm 0.042$	$91066.8 \pm 3464.2$
424.5	H	7.8	$10.177 \pm 0.042$	$86920.1 \pm 3306.4$
432.4	H	7.8	$10.245 \pm 0.042$	$81665.8 \pm 3107.6$
344.0	K <sub>s</sub>	7.8	$9.067 \pm 0.058^{\text{x}}$	$157495.6 \pm 8197.4^{\text{x}}$
352.3	K <sub>s</sub>	7.8	$9.308 \pm 0.058^{\text{x}}$	$126102.6 \pm 6564.2^{\text{x}}$
360.2	K <sub>s</sub>	7.8	$9.207 \pm 0.058^{\text{x}}$	$138421.8 \pm 7205.9^{\text{x}}$
380.1	K <sub>s</sub>	7.8	$9.312 \pm 0.058$	$125650.6 \pm 6541.1$
388.4	K <sub>s</sub>	7.8	$9.310 \pm 0.058$	$125949.5 \pm 6557.6$
396.3	K <sub>s</sub>	7.8	$9.419 \pm 0.058$	$113840.4 \pm 5927.9$
416.3	K <sub>s</sub>	7.8	$9.508 \pm 0.058$	$104946.6 \pm 5465.3$
424.5	K <sub>s</sub>	7.8	$9.546 \pm 0.058$	$101331.5 \pm 5277.5$
432.4	K <sub>s</sub>	7.8	$9.638 \pm 0.058$	$93031.2 \pm 4845.6$

Note. — Because of the very large number of exposures acquired, only a few representative points are given. The full table of photometry containing all 406 points is available online. Includes only

non-saturated exposures; photometry from the saturated epochs is given in Tables 2 and 3.

<sup>a</sup>Exposure mid-time, measured from the *Swift* trigger (UTC 06:12:49).

<sup>b</sup>Observed value; not corrected for Galactic extinction.

<sup>x</sup>Point not used in modeling.

Table 2. PAIRITEL Short-Read Observations of GRB 080319B During Saturated Regime

$t_{\text{mid}}^{\text{a}}$ sec	Filter	Exp. time sec	Mag. <sup>b</sup>	Flux <sup>b</sup> $\mu\text{Jy}$
59.3	J	0.051	$5.206 \pm 0.055$	$1.32 \times 10^7 \pm 6.52 \times 10^5$
67.3	J	0.051	$5.627 \pm 0.055$	$8.94 \times 10^6 \pm 4.43 \times 10^5$
87.3	J	0.051	$6.470 \pm 0.055$	$4.11 \times 10^6 \pm 2.04 \times 10^5$
95.5	J	0.051	$6.847 \pm 0.056$	$2.91 \times 10^6 \pm 1.45 \times 10^5$
103.5	J	0.051	$6.954 \pm 0.056$	$2.63 \times 10^6 \pm 1.32 \times 10^5$
59.3	H	0.051	$4.520 \pm 0.052$	$1.59 \times 10^7 \pm 7.47 \times 10^5$
67.3	H	0.051	$4.853 \pm 0.052$	$1.17 \times 10^7 \pm 5.50 \times 10^5$
87.3	H	0.051	$5.713 \pm 0.052$	$5.30 \times 10^6 \pm 2.50 \times 10^5$
95.5	H	0.051	$6.101 \pm 0.052$	$3.71 \times 10^6 \pm 1.75 \times 10^5$
103.5	H	0.051	$6.225 \pm 0.052$	$3.31 \times 10^6 \pm 1.56 \times 10^5$
67.3	$K_s$	0.051	$4.362 \pm 0.048$	$1.20 \times 10^7 \pm 5.20 \times 10^5$
87.3	$K_s$	0.051	$5.192 \pm 0.048$	$5.59 \times 10^6 \pm 2.43 \times 10^5$
95.5	$K_s$	0.051	$5.308 \pm 0.048$	$5.02 \times 10^6 \pm 2.18 \times 10^5$
103.5	$K_s$	0.051	$5.675 \pm 0.048$	$3.58 \times 10^6 \pm 1.56 \times 10^5$

<sup>a</sup>Exposure mid-time, measured from the *Swift* trigger (UT 06:12:49).

<sup>b</sup>Observed value; not corrected for Galactic extinction.

<sup>x</sup>No saturated values were used in modeling.

Note. — Because of the large number of exposures acquired, only a few representative points are given. The full table of photometry containing all 406 points is available online.

Table 3. PAIRITEL Annulus Photometry of GRB 080319B During Saturated Regime

$t_{\text{mid}}^{\text{a}}$ sec	Filter	Exp. time sec	Mag. <sup>b</sup>	Flux <sup>b</sup> $\mu\text{Jy}$
55.0	J	7.8	$4.595 \pm 0.133$	$2.31 \times 10^7 \pm 2.66 \times 10^6$
63.2	J	7.8	$5.070 \pm 0.133$	$1.49 \times 10^7 \pm 1.72 \times 10^6$
71.2	J	7.8	$5.560 \pm 0.133$	$9.51 \times 10^6 \pm 1.10 \times 10^6$
91.2	J	7.8	$6.572 \pm 0.133$	$3.74 \times 10^6 \pm 4.31 \times 10^5$
99.4	J	7.8	$6.710 \pm 0.133$	$3.30 \times 10^6 \pm 3.80 \times 10^5$
107.4	J	7.8	$7.004 \pm 0.133$	$2.51 \times 10^6 \pm 2.90 \times 10^5$
55.0	H	7.8	$4.387 \pm 0.191$	$1.80 \times 10^7 \pm 2.90 \times 10^6$
63.2	H	7.8	$4.805 \pm 0.191$	$1.22 \times 10^7 \pm 1.97 \times 10^6$
71.2	H	7.8	$5.159 \pm 0.191$	$8.84 \times 10^6 \pm 1.42 \times 10^6$
91.2	H	7.8	$5.818 \pm 0.191$	$4.82 \times 10^6 \pm 7.76 \times 10^5$
99.4	H	7.8	$6.386 \pm 0.191$	$2.86 \times 10^6 \pm 4.60 \times 10^5$
107.4	H	7.8	$6.421 \pm 0.191$	$2.76 \times 10^6 \pm 4.45 \times 10^5$
55.0	$K_s$	7.8	$3.853 \pm 0.463$	$1.92 \times 10^7 \pm 6.65 \times 10^6$
63.2	$K_s$	7.8	$4.200 \pm 0.463$	$1.39 \times 10^7 \pm 4.83 \times 10^6$
71.2	$K_s$	7.8	$4.510 \pm 0.463$	$1.05 \times 10^7 \pm 3.63 \times 10^6$
91.2	$K_s$	7.8	$5.130 \pm 0.463$	$5.91 \times 10^6 \pm 2.05 \times 10^6$
99.4	$K_s$	7.8	$5.659 \pm 0.463$	$3.63 \times 10^6 \pm 1.26 \times 10^6$
107.4	$K_s$	7.8	$5.812 \pm 0.463$	$3.16 \times 10^6 \pm 1.09 \times 10^6$

<sup>a</sup>Exposure mid-time, measured from the *Swift* trigger (UT 06:12:49).

<sup>b</sup>Observed value; not corrected for Galactic extinction.

<sup>x</sup>No saturated values were used in modeling.

Note. — Because of the large number of exposures acquired, only a few representative points are given. The full table of photometry containing all 406 points is available online.

Table 4. KAIT Observations of GRB 080319B

$t_{\text{mid}}^{\text{a}}$ sec	Filter	Exp. time sec	Mag. <sup>b</sup>	Flux <sup>b</sup> $\mu\text{Jy}$
1217.0	clear	20.0	$14.116 \pm 0.008$	$7008.1 \pm 51.4$
1308.0	clear	20.0	$14.261 \pm 0.007$	$6132.0 \pm 39.4$
1404.0	clear	20.0	$14.424 \pm 0.011$	$5277.2 \pm 53.2$
1495.0	clear	20.0	$14.548 \pm 0.013$	$4707.6 \pm 56.0$
1586.0	clear	20.0	$14.651 \pm 0.011$	$4281.5 \pm 43.2$
2098.0	B	20.0	$15.623 \pm 0.045$	$2327.0 \pm 94.5$
2249.0	B	20.0	$15.750 \pm 0.041$	$2070.1 \pm 76.7$
2373.0	B	20.0	$15.814 \pm 0.042$	$1951.6 \pm 74.1$
2546.5	B	40.0	$15.911 \pm 0.037$	$1784.8 \pm 59.8$
2791.0	B	40.0	$16.094 \pm 0.035$	$1508.0 \pm 47.8$
1157.0	V	20.0	$14.345 \pm 0.022$	$6745.3 \pm 135.3$
1248.0	V	20.0	$14.442 \pm 0.022$	$6168.8 \pm 123.7$
1339.0	V	20.0	$14.651 \pm 0.022$	$5088.6 \pm 102.1$
1435.0	V	20.0	$14.815 \pm 0.025$	$4375.2 \pm 99.6$
1526.0	V	20.0	$14.939 \pm 0.026$	$3903.0 \pm 92.4$
1188.0	I	20.0	$13.777 \pm 0.013$	$7502.4 \pm 89.3$
1279.0	I	20.0	$13.879 \pm 0.012$	$6829.7 \pm 75.1$
1370.0	I	20.0	$14.016 \pm 0.015$	$6020.0 \pm 82.6$
1465.0	I	20.0	$14.176 \pm 0.020$	$5195.2 \pm 94.8$
1557.0	I	20.0	$14.328 \pm 0.018$	$4516.5 \pm 74.3$

Note. — Because of the very large number of exposures acquired, only the first five exposures in each band are given. The full table of photometry is available online.

<sup>a</sup>Exposure mid-time, measured from the *Swift* trigger (UTC 06:12:49).

<sup>b</sup>Observed value; not corrected for Galactic extinction.

Table 5. Nickel Observations of GRB 080319B

$t_{\text{mid}}^{\text{a}}$ sec	Filter	Exp. time sec	Mag. <sup>b</sup>	Flux <sup>b</sup> $\mu\text{Jy}$
7154.7	B	360.0	$17.365 \pm 0.005$	$467.7 \pm 2.1$
8579.2	B	360.0	$17.646 \pm 0.006$	$361.1 \pm 2.0$
10013.4	B	360.0	$17.866 \pm 0.008$	$294.8 \pm 2.2$
11512.3	B	360.0	$18.090 \pm 0.008$	$239.9 \pm 1.8$
13015.9	B	360.0	$18.248 \pm 0.011$	$207.4 \pm 2.1$
14473.6	B	360.0	$18.389 \pm 0.011$	$182.1 \pm 1.8$
16436.8	B	360.0	$18.587 \pm 0.015$	$151.8 \pm 2.1$
17937.4	B	360.0	$18.770 \pm 0.018$	$128.2 \pm 2.1$
19398.1	B	360.0	$18.858 \pm 0.015$	$118.2 \pm 1.6$
20965.3	B	360.0	$18.970 \pm 0.023$	$106.7 \pm 2.2$
7444.0	V	300.0	$17.251 \pm 0.005$	$464.1 \pm 2.1$
8860.5	V	300.0	$17.484 \pm 0.007$	$374.5 \pm 2.4$
10291.9	V	300.0	$17.727 \pm 0.007$	$299.4 \pm 1.9$
11829.3	V	300.0	$17.899 \pm 0.007$	$255.5 \pm 1.6$
13294.2	V	300.0	$18.062 \pm 0.007$	$219.9 \pm 1.4$
14767.2	V	300.0	$18.236 \pm 0.014$	$187.3 \pm 2.4$
16714.4	V	300.0	$18.424 \pm 0.012$	$157.5 \pm 1.7$
18236.5	V	300.0	$18.559 \pm 0.016$	$139.1 \pm 2.0$
19700.4	V	300.0	$18.637 \pm 0.013$	$129.5 \pm 1.5$
22996.8	V	300.0	$18.902 \pm 0.021$	$101.4 \pm 1.9$
7782.0	R	300.0	$16.991 \pm 0.006$	$496.1 \pm 2.7$
9196.4	R	300.0	$17.239 \pm 0.005$	$394.8 \pm 1.8$
10635.4	R	300.0	$17.435 \pm 0.008$	$329.6 \pm 2.4$
12181.0	R	300.0	$17.637 \pm 0.009$	$273.7 \pm 2.3$
13652.0	R	300.0	$17.799 \pm 0.007$	$235.7 \pm 1.5$
15110.2	R	300.0	$17.917 \pm 0.007$	$211.4 \pm 1.4$
17071.9	R	300.0	$18.107 \pm 0.011$	$177.5 \pm 1.8$
18582.1	R	300.0	$18.218 \pm 0.008$	$160.3 \pm 1.2$
20035.8	R	300.0	$18.308 \pm 0.017$	$147.5 \pm 2.3$
23331.8	R	300.0	$18.541 \pm 0.021$	$119.0 \pm 2.3$
8122.0	I	300.0	$16.797 \pm 0.004$	$464.7 \pm 1.7$

Table 5—Continued

$t_{\text{mid}}^{\text{a}}$ sec	Filter	Exp. time sec	Mag. <sup>b</sup>	Flux <sup>b</sup> $\mu\text{Jy}$
9531.2	I	300.0	$17.013 \pm 0.005$	$380.9 \pm 1.7$
10995.4	I	300.0	$17.189 \pm 0.005$	$323.9 \pm 1.5$
12520.7	I	300.0	$17.394 \pm 0.005$	$268.2 \pm 1.2$
14003.3	I	300.0	$17.537 \pm 0.009$	$235.1 \pm 1.9$
15973.2	I	300.0	$17.704 \pm 0.008$	$201.6 \pm 1.5$
17412.9	I	300.0	$17.817 \pm 0.011$	$181.6 \pm 1.8$
18936.7	I	300.0	$17.921 \pm 0.010$	$165.0 \pm 1.5$
20447.9	I	300.0	$18.045 \pm 0.014$	$147.2 \pm 1.9$
23665.5	I	300.0	$18.111 \pm 0.118$	$138.5 \pm 14.3$

<sup>a</sup>Exposure mid-time, measured from the *Swift* trigger (UTC 06:12:49).

<sup>b</sup>Observed value; not corrected for Galactic extinction.

Table 6. UVOT Observations of GRB 080319B

$t_{\text{mid}}^{\text{a}}$ sec	Filter	Exp. time sec	Mag. <sup>b</sup>	Flux <sup>b</sup> $\mu\text{Jy}$
6156.0	UVW1	196.6	$16.146 \pm 0.043$	$343.2 \pm 13.3$
17398.0	UVW1	885.6	$17.645 \pm 0.042$	$86.3 \pm 3.3$
28047.0	UVW1	427.9	$18.316 \pm 0.086$	$46.5 \pm 3.5$
45393.0	UVW1	427.9	$18.909 \pm 0.121$	$26.9 \pm 2.8$
75628.0	UVW1	200.6	$19.266 \pm 0.213$	$19.4 \pm 3.5$
5542.0	UVW2	196.6	$16.192 \pm 0.046$	$239.6 \pm 9.9$
10709.0	UVW2	885.6	$17.231 \pm 0.036$	$92.0 \pm 3.0$
22273.0	UVW2	266.3	$18.394 \pm 0.116$	$31.5 \pm 3.2$
28931.0	UVW2	856.1	$18.631 \pm 0.073$	$25.3 \pm 1.6$
46279.0	UVW2	856.1	$19.228 \pm 0.102$	$14.6 \pm 1.3$
76050.0	UVW2	401.3	$19.888 \pm 0.220$	$8.0 \pm 1.5$
5951.0	UVM2	196.6	$15.923 \pm 0.052$	$284.4 \pm 13.3$
12528.0	UVM2	334.6	$17.144 \pm 0.071$	$92.4 \pm 5.8$
16491.0	UVM2	885.6	$17.493 \pm 0.052$	$67.0 \pm 3.1$
30028.0	UVM2	611.2	$18.381 \pm 0.101$	$29.6 \pm 2.6$
47376.0	UVM2	610.0	$19.039 \pm 0.144$	$16.1 \pm 2.0$
631.0	U	19.4	$12.474 \pm 0.028^{\text{x}}$	$19697.0 \pm 501.5^{\text{x}}$
785.0	U	19.4	$12.968 \pm 0.030$	$12496.8 \pm 340.6$
1430.0	U	19.4	$14.108 \pm 0.042$	$4373.2 \pm 165.9$
1591.0	U	19.5	$14.342 \pm 0.046$	$3525.3 \pm 146.2$
4926.0	U	196.6	$16.015 \pm 0.029$	$755.1 \pm 19.9$
6362.0	U	196.6	$16.329 \pm 0.033$	$565.5 \pm 16.9$
18304.0	U	295.0	$17.864 \pm 0.056$	$137.5 \pm 6.9$
18609.0	U	231.2	$17.886 \pm 0.064$	$134.8 \pm 7.7$
28486.0	U	213.4	$18.498 \pm 0.089$	$76.7 \pm 6.0$
45833.0	U	213.4	$19.435 \pm 0.148$	$32.4 \pm 4.1$
656.0	B	9.6	$13.334 \pm 0.042^{\text{x}}$	$19160.2 \pm 727.0^{\text{x}}$
811.0	B	9.6	$13.913 \pm 0.046$	$11240.9 \pm 466.3$
1454.0	B	19.4	$15.012 \pm 0.046$	$4085.1 \pm 169.5$
1616.0	B	19.5	$15.291 \pm 0.052$	$3159.4 \pm 147.7$
5131.0	B	196.6	$16.962 \pm 0.033$	$678.0 \pm 20.3$
6567.0	B	196.6	$17.350 \pm 0.039$	$474.2 \pm 16.7$



Table 6—Continued

$t_{\text{mid}}^{\text{a}}$ sec	Filter	Exp. time sec	Mag. <sup>b</sup>	Flux <sup>b</sup> $\mu\text{Jy}$
28708.0	B	213.4	$19.417 \pm 0.112$	$70.7 \pm 6.9$
46055.0	B	213.3	$20.036 \pm 0.171$	$40.0 \pm 5.8$
75943.0	B	100.2	$20.441 \pm 0.316$	$27.5 \pm 6.9$
711.0	V	19.5	$13.373 \pm 0.040^{\text{x}}$	$16512.0 \pm 597.2^{\text{x}}$
975.0	V	393.5	$14.337 \pm 0.013^{\text{x}}$	$6795.2 \pm 80.9^{\text{x}}$
1518.0	V	19.4	$15.025 \pm 0.076$	$3605.8 \pm 243.8$
1680.0	V	19.5	$15.127 \pm 0.081$	$3282.5 \pm 236.0$
5746.0	V	196.6	$16.955 \pm 0.058$	$609.5 \pm 31.7$
11616.0	V	295.0	$17.948 \pm 0.078$	$244.2 \pm 16.9$
11919.0	V	295.1	$17.895 \pm 0.078$	$256.4 \pm 17.8$
12222.0	V	295.0	$18.041 \pm 0.082$	$224.2 \pm 16.3$
29806.0	V	213.4	$19.491 \pm 0.256$	$59.0 \pm 12.4$

<sup>a</sup>Exposure mid-time, measured from the *Swift* trigger (UTC 06:12:49).

<sup>b</sup>Observed value; not corrected for Galactic extinction.

<sup>x</sup>Point not used in modeling.

Table 7. Gemini Observations of GRB 080319B

$t_{\text{mid}}^{\text{a}}$ sec	Filter	Exp. time sec	Mag. <sup>b</sup>	Flux <sup>b</sup> $\mu\text{Jy}$
89309	g	$5 \times 180$	$20.670 \pm 0.100$	$19.59 \pm 1.72$
90356	r	$5 \times 180$	$20.520 \pm 0.060$	$22.49 \pm 1.21$
91307	i	$5 \times 180$	$20.380 \pm 0.050$	$25.59 \pm 1.15$
92470	z	$5 \times 180$	$20.310 \pm 0.050$	$27.93 \pm 1.26$
174960	r	$5 \times 180$	$21.510 \pm 0.060$	$9.037 \pm 0.486$
520390	g	$6 \times 180$	$23.450 \pm 0.190$	$1.514 \pm 0.243$
521589	r	$6 \times 180$	$23.340 \pm 0.090$	$1.675 \pm 0.133$
522792	i	$6 \times 180$	$22.900 \pm 0.060$	$2.512 \pm 0.135$
523990	z	$6 \times 180$	$22.940 \pm 0.090$	$2.477 \pm 0.197$
780120	r	$6 \times 180$	$23.670 \pm 0.070$	$1.236 \pm 0.077$
781560	i	$6 \times 180$	$23.280 \pm 0.060$	$1.770 \pm 0.095$
1209960	g	$6 \times 180$	$24.440 \pm 0.080$	$0.6081 \pm 0.0432$
1211220	r	$6 \times 180$	$24.100 \pm 0.080$	$0.8318 \pm 0.0591$
1212480	i	$6 \times 180$	$23.810 \pm 0.070$	$1.086 \pm 0.068$
2286720	g	$6 \times 180$	$25.860 \pm 0.110^{\text{x}}$	$0.1644 \pm 0.0158^{\text{x}}$
2287800	r	$6 \times 180$	$25.050 \pm 0.090^{\text{x}}$	$0.3467 \pm 0.0276^{\text{x}}$
2285280	i	$6 \times 180$	$24.360 \pm 0.080^{\text{x}}$	$0.6546 \pm 0.0465^{\text{x}}$
2531160	z	$3 \times 180$	$23.940 \pm 0.130^{\text{x}}$	$0.9863 \pm 0.1113^{\text{x}}$

<sup>a</sup>Exposure mid-time, measured from the *Swift* trigger (UTC 06:12:49).

<sup>b</sup>Observed value; not corrected for Galactic extinction.

<sup>x</sup>Point not used in modeling.

Table 8. GCN Observations of GRB 080319B

$t_{\text{mid}}^{\text{a}}$ sec	Filter	Exp. time sec	Mag. <sup>b</sup>	Flux <sup>b</sup> $\mu\text{Jy}$		
-11.0	clear	10.0	$\geq 11.48$	$\leq 7.94 \times 10^4$	Pi <sup>c</sup>	GCN 7445 <sup>d</sup>
3.0	clear	10.0	9.83	$3.63 \times 10^5$	Pi	GCN 7445
17.0	clear	10.0	5.76	$1.54 \times 10^7$	Pi	GCN 7445
32.0	clear	10.0	6.00	$1.24 \times 10^7$	Pi	GCN 7445
79.0	clear	10.0	8.26	$1.54 \times 10^6$	Pi	GCN 7445
93.0	clear	10.0	8.77	$9.64 \times 10^5$	Pi	GCN 7445
108.0	clear	10.0	9.10	$7.11 \times 10^5$	Pi	GCN 7445
122.0	clear	10.0	10.27	$2.42 \times 10^5$	Pi	GCN 7445
163.0	clear	10.0	10.50	$1.96 \times 10^5$	Pi	GCN 7445
177.0	clear	10.0	11.10	$1.13 \times 10^5$	Pi	GCN 7445
252.0	clear	10.0	11.21	$1.02 \times 10^5$	Pi	GCN 7445
296.0	clear	10.0	11.79	$5.97 \times 10^4$	Pi	GCN 7445
310.0	clear	10.0	11.95	$5.15 \times 10^4$	Pi	GCN 7445
37.2	clear	10.0	5.60	$1.79 \times 10^7$	RAPTOR	GCN 7464 <sup>e</sup>
24.6	clear	5.0	5.35	$2.25 \times 10^7$	ROTSE	GCN 7470 <sup>f</sup>
111.7	clear	20.0	8.49	$1.25 \times 10^6$	ROTSE	GCN 7470
8.9	clear <sup>v</sup>	–	$8.198 \pm 0.579$	$1.94 \times 10^6 \pm 8.02 \times 10^5$	TORTORA	GCN 7558 <sup>g</sup>
10.1	clear <sup>v</sup>	–	$6.967 \pm 0.188$	$6.03 \times 10^6 \pm 9.58 \times 10^5$	TORTORA	GCN 7558
11.5	clear <sup>v</sup>	–	$6.650 \pm 0.141$	$8.07 \times 10^6 \pm 9.83 \times 10^5$	TORTORA	GCN 7558
60300.0	R	–	19.80	$3.73 \times 10^1$	Canarias	GCN 7476 <sup>h</sup>
55830.0	clear	1500.0	$19.080 \pm 0.020$	$7.24 \times 10^1 \pm 1.32 \times 10^0$	AAVSO	GCN 7484 <sup>i</sup>
70500.0	clear	2040.0	$19.000 \pm 0.100$	$7.80 \times 10^1 \pm 6.86 \times 10^0$	AAVSO	GCN 7484
74831.0	R	–	$20.000 \pm 0.300$	$3.10 \times 10^1 \pm 7.50 \times 10^0$	Brno	GCN 7504 <sup>j</sup>
43934.4	R	–	19.10	$7.11 \times 10^1$	Kharkiv	GCN 7519 <sup>k</sup>
46270.8	R	–	19.90	$3.40 \times 10^1$	Kharkiv	GCN 7519
71208.0	R	–	20.10	$2.83 \times 10^1$	Kharkiv	GCN 7519
1656000	R <sup>n</sup>	–	24.35	$5.65 \times 10^{-1}$	HST	GCN 7569 <sup>l</sup>
1656000	I <sup>o</sup>	–	23.76	$7.62 \times 10^{-1}$	HST	GCN 7569
4590000	R <sup>n</sup>	–	$26.280 \pm 0.100$	$9.55 \times 10^{-2} \pm 8.40 \times 10^{-3}$	HST	GCN 7710 <sup>m</sup>
4590000	I <sup>o</sup>	–	$25.460 \pm 0.100$	$1.59 \times 10^{-1} \pm 1.40 \times 10^{-2}$	HST	GCN 7710

Note. — Most of the TORTORA measurements have been omitted to save space. The full table of GCN photometry used in our plot is available online.

<sup>a</sup>Exposure mid-time, measured from the *Swift* trigger (UTC 06:12:49).

<sup>b</sup>Observed value; not corrected for Galactic extinction.

<sup>c</sup>“Pi-of-the-Sky” Collaboration

<sup>d</sup>Cwiok et al. (2008a)

<sup>e</sup>Wozniak et al. (2008)

<sup>f</sup>Swan et al. (2008)

<sup>g</sup>Karpov et al. (2008b)

<sup>h</sup>Jelinek et al. (2008)

<sup>i</sup>Hentunen et al. (2008)

<sup>j</sup>Novak (2008)

<sup>k</sup>Krugly et al. (2008)

<sup>l</sup>Tanvir et al. (2008)

<sup>m</sup>Levan et al. (2008)

<sup>n</sup>Converted from F606W.

<sup>o</sup>Converted from F804W.

<sup>v</sup>Calibrated to *V*-band and plotted as *V* in our figures.

<sup>x</sup>No GCN observations were used in modeling.

Table 9. Bright SDSS standard stars

RA deg	Dec deg	B mag	V mag	R mag	I mag
217.915229	36.31513	15.940 ± 0.010	15.293 ± 0.006	14.922 ± 0.008	14.551 ± 0.007
217.908143	36.29125	17.716 ± 0.012	16.350 ± 0.006	15.523 ± 0.008	14.821 ± 0.007
217.943617	36.31667	17.993 ± 0.012	16.834 ± 0.006	16.162 ± 0.008	15.590 ± 0.007

Table 10. Faint SDSS standard stars

RA deg	Dec deg	g mag	r mag	i mag	z mag
217.908143	36.29125	17.091 ± 0.005	15.816 ± 0.004	15.310 ± 0.004	15.067 ± 0.005
217.943617	36.31667	17.425 ± 0.005	16.409 ± 0.004	16.058 ± 0.004	15.872 ± 0.007
217.871828	36.29380	17.364 ± 0.005	16.903 ± 0.005	16.769 ± 0.005	16.689 ± 0.010
217.894280	36.34851	18.298 ± 0.007	16.955 ± 0.005	16.370 ± 0.005	16.036 ± 0.007
217.902832	36.33332	18.084 ± 0.006	17.741 ± 0.006	17.626 ± 0.007	17.565 ± 0.017
217.981086	36.29605	18.223 ± 0.007	17.866 ± 0.006	17.746 ± 0.008	17.723 ± 0.041
217.931339	36.34208	19.812 ± 0.014	18.342 ± 0.008	16.818 ± 0.005	16.016 ± 0.007
217.931216	36.27044	19.172 ± 0.010	18.382 ± 0.008	18.110 ± 0.009	17.988 ± 0.021
217.918619	36.31995	20.742 ± 0.026	19.264 ± 0.013	18.483 ± 0.011	18.055 ± 0.024
217.913905	36.28612	20.736 ± 0.027	19.266 ± 0.013	18.253 ± 0.010	17.687 ± 0.019
217.928915	36.33948	20.850 ± 0.029	19.462 ± 0.017	18.214 ± 0.010	17.578 ± 0.018
217.928801	36.30674	20.844 ± 0.028	19.471 ± 0.014	18.689 ± 0.012	18.315 ± 0.029
217.955190	36.33084	19.708 ± 0.014	19.506 ± 0.015	19.505 ± 0.023	19.315 ± 0.065
217.926000	36.33788	20.047 ± 0.016	19.640 ± 0.016	19.474 ± 0.022	19.437 ± 0.071
217.932586	36.27256	21.248 ± 0.033	19.710 ± 0.016	18.342 ± 0.010	17.551 ± 0.016
217.946853	36.30972	21.362 ± 0.040	19.909 ± 0.020	19.003 ± 0.016	18.439 ± 0.033
217.971356	36.30059	21.318 ± 0.039	19.937 ± 0.020	19.043 ± 0.016	18.571 ± 0.035